Final Report

a. Federal Agency	Department of Energy	
b. Award Number	DE-EE0008982	
c. Sponsoring Program Office	Solar Energy Technologies Office	
d. Project Title	III-V Solar Cells with Novel Epitaxial Lift-off Architectures for Extended Substrate Reuse for Low-cost Manufacturing	
e. Principal Investigator	Name: Venkat Selvamanickam	
f. Submission Date	09-04-22	
g. DUNS Number	03683792	
h. Recipient Organization	University of Houston	
i. Project Period	**Start**: 03-01-20	**End**: 08-31-21

Acknowledgement: This material is based upon work supported by the Department of Energy, Office of Energy Efficiency and Renewable Energy, Solar Energy Technologies Office, under Award Number DE-EE0008982.

Major Goals & Objectives:

The objective of this project is the development of a novel epitaxial lift-off (ELO) architecture for single junction gallium arsenide (GaAs) solar cells that will not require chemical mechanical polishing (CMP) of the substrate for re-use. Our goal is to demonstrate 20% efficient GaAs solar cells with ARC (stretch goal of 25% efficient cells) with less than 10% reduction in conversion efficiency after 25 substrate re-uses without CMP and before lift-off.

The main tasks in this project are:

1. Growth and fabrication of GaAs solar cells with water-soluble ELO sacrificial buffer
2. Optimization of ELO process with water-soluble sacrificial buffer
3. Regrowth and fabrication of GaAs solar cells after ELO without CMP
4. Improvement of conversion efficiency of GaAs solar cells with ELO architecture

D. Project Management

Project Results and Discussion:

Task 1.0: Growth and fabrication of GaAs solar cells with water-soluble ELO sacrificial buffer

Subtask 1.1: Growth of water-soluble ELO sacrificial buffer on GaAs wafer

A water-soluble sacrificial NaCl layer was deposited by magnetron sputtering on an epi-ready Ge & GaAs wafers using 99.99% purity NaCl target. NaCl has to be epitaxially grown with a smooth morphology for subsequent growth of GaAs films by metal organic chemical vapor deposition (MOCVD) for device fabrication. NaCl was deposited at room temperature to first confirm the formation of NaCl film on a Ge wafer. Figure 1 shows 2-Dimensional X-Ray Diffraction (2DXRD) results as a function of deposition time. The strongest peak at 66º corresponds to the Ge/NaCl (400) reflections, and the signal at 33º is indicative of the presence of NaCl (200). Since (200) is forbidden in Ge, the presence of a reflection at 33º confirms that it belongs only to NaCl. Note that on GaAs wafer, the peaks of GaAs and NaCl will coincide making it difficult to discern the presence of NaCl. The streaking at 33º further suggests that it is from NaCl as the signal along the chi direction in 2DXRD indicates a distribution of reflections that satisfy the Bragg condition, meaning that the sample is polycrystalline. Since the Ge wafer is confirmed to be a single-crystal substrate, it is not possible for the intensity distribution to arise from the wafer. The increase of intensity of the chi spread over time also confirms that these reflections are from NaCl as more material is deposited on the wafer.

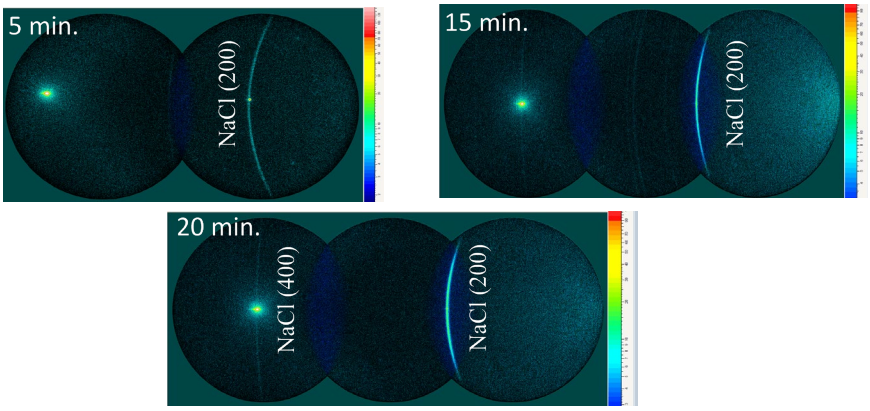

Figure 1. *2DXRD measurements of NaCl deposited at room temperature for: (top left) 5 minutes, (top right) 15 minutes, and (bottom) 20 minutes.*

Once the deposition of NaCl was confirmed, the effect of temperature was studied as it is a key parameter that determines the film morphology and crystal quality during sputter deposition. Figure 2 summarizes the temperature dependent data. Upon increasing temperature and maintaining the deposition time same, the only feature that is noticeably changed in the 2DXRD data is the chi spread. As the temperature is increased, the chi spread decreases, indicating an improvement in the crystal quality of the film. At the highest deposition temperature of 700°C, the smallest chi spread is seen and it matches the chi spread as the original wafer.

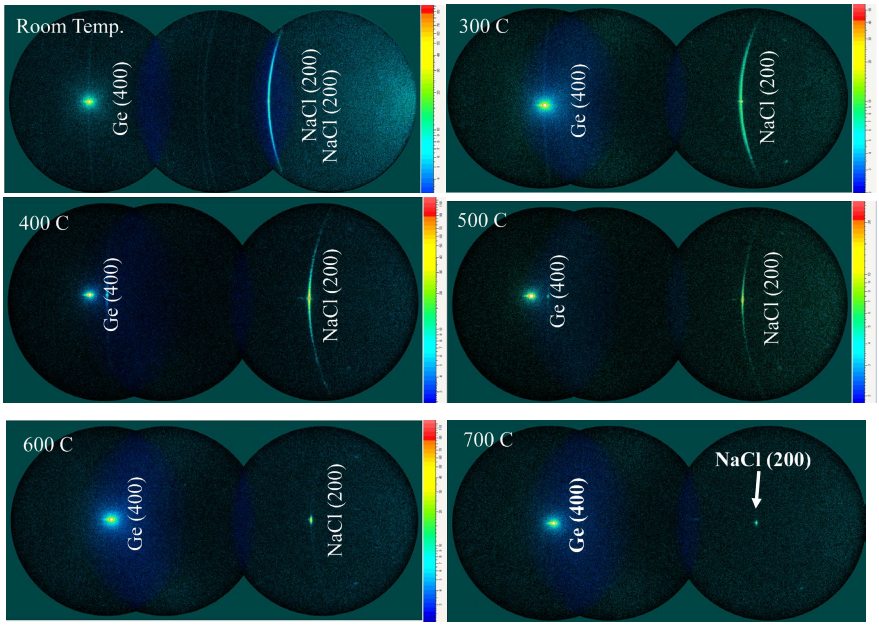

Figure 2. *2DXRD data showing the temperature dependence of NaCl deposited on Ge wafer.*

For all samples after deposition, there is a clear color difference on the film surface, which is another indicator of successful NaCl deposition. SEM images of select samples

are shown on Figure 3. In samples deposited at lower temperatures, the NaCl film appears to be a porous structure characterized by isolated NaCl islands that confirms their island growth mechanism. The presence of these island structures reinforces the 2DXRD data where the NaCl is randomly distributed on the surface of the Ge wafer. Upon increasing the deposition temperature to 400°C, the islands appear to be more packed together, but the NaCl still appears to be deposited in as island manner. However, at high temperatures, the morphology of the NaCl film appears to be smooth which confirms the layer-by-layer growth mechanism of NaCl film, indicating that the NaCl is replicating the single-crystal Ge wafer structure, as confirmed by 2DXRD.

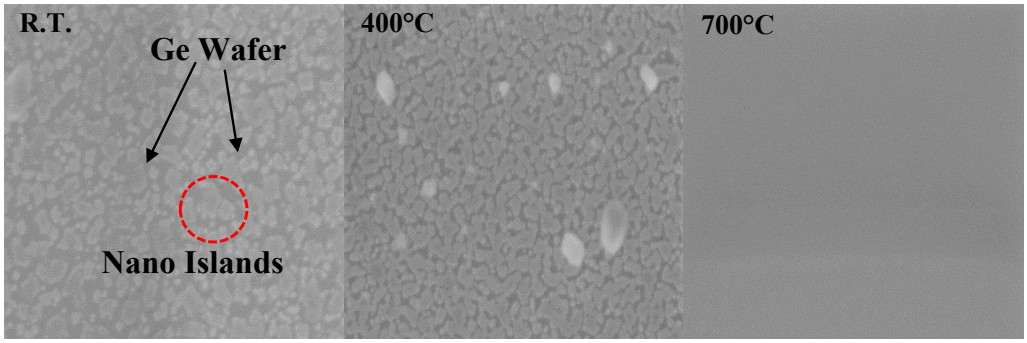

Figure 3. *SEM micrographs of NaCl films deposited on Ge wafers at different temperatures.*

Figure 4(a) shows the 2-Dimensional X-Ray Diffraction (2D-XRD) result of NaCl deposited at 700ºC on Ge wafer. The peak observed 31.7º corresponds to NaCl (200), and that at 66.3º is Ge (400) from the wafer substrate. An integration of the 2D-XRD data is shown in figure 4(b) which reveals that the intensity of NaCl (200) is greater than 90% of sum intensity of all NaCl peaks. A protective Ge cap layer was deposited in the same magnetron sputtering tool on the NaCl film to avoid exposure to atmosphere/moisture that can degrade the NaCl film during sample transfer for GaAs device processing in the MOCVD tool. 2D-XRD analysis on the Ge film on NaCl showed that the Ge is also epitaxial with (200) orientation.

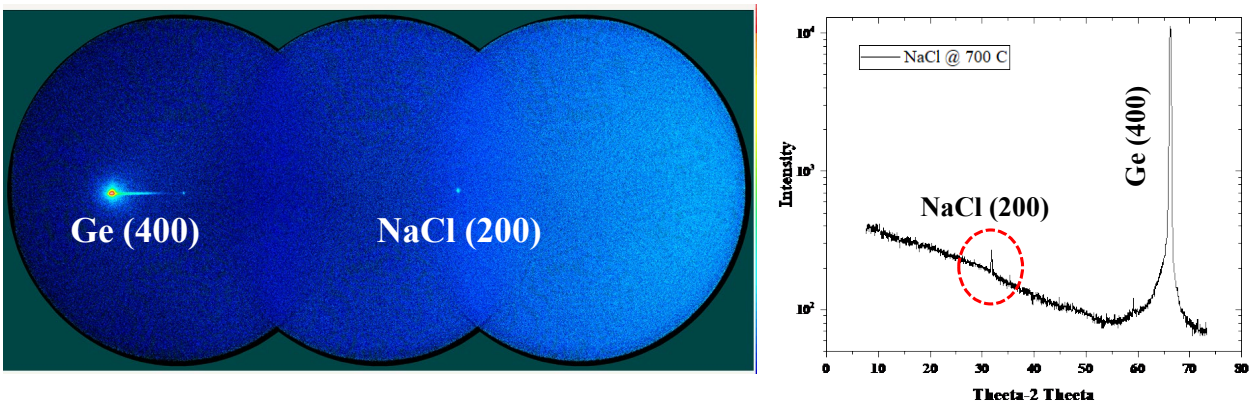

Figure 4. *(Left) 2D XRD data of NaCl grown on Ge wafer. Only (200) orientation of NaCl at 31.7° is seen. (b) Line integration of the 2D-XRD data showing that the intensity of NaCl (200) is greater than 90% of sum intensity of all NaCl peaks.*

The Ge/NaCl/Ge wafer samples were then used for GaAs growth by MOCVD and solar cell device fabrication as discussed in subtasks 1.2 and 1.3 of this report. The solar cell device exhibited conversion efficiency of 11% (Figure 25). The solar cell device sample was immersed in water, no lift-off was observed, contrary to our findings of liftoff of films after NaCl growth. As described in subtask 1.2, SIMS analysis of the GaAs solar cell device (Figure 17) showed the presence of Na and Cl in the architecture. Transmission Electron Microscopy (TEM) results (Figure 18) however indicated that the NaCl layer is very thin ~ 2 nm, which could be the reason for no lift off.

In an effort to preserve the integrity and solubility of NaCl after device fabrication, we proceeded to deposit NaCl at a lower temperature of 600ºC. Figure 5 shows the 2D-XRD results featuring a single NaCl (200) peak confirming epitaxy. A protective Ge cap layer was grown on the NaCl film. When immersed in water, we were able confirm liftoff of the Ge film. Prior to liftoff, the cross section of the sample was analyzed by TEM which confirmed the presence of the NaCl film (Figure 6). The NaCl film was found to be substantially thicker (25 nm) compared to the thin 2 nm thick NaCl film grown at 700ºC and observed after GaAs device fabrication.

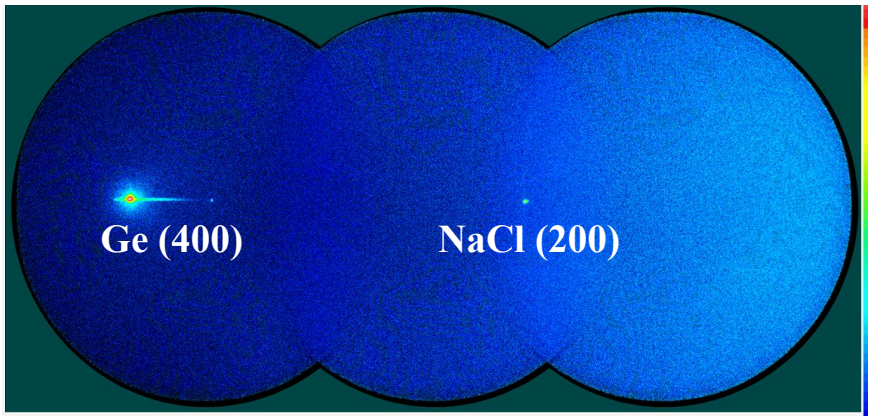

Figure 5. *2D XRD data of NaCl grown on Ge wafer at 600°C. Only (200) orientation of NaCl at 31.7° is seen along with Ge (400) wafer peak at 66.3 °.*

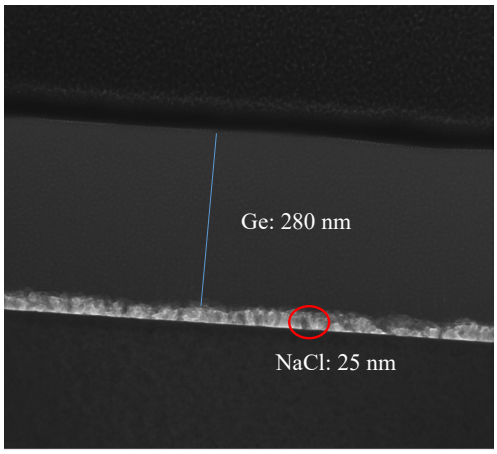

Figure 6. *Cross section TEM micrograph of Ge film on NaCl deposited on Ge wafer.*

A GaAs film was grown by MOCVD on the Ge film described in Figure 3. We were able to successfully lift off the GaAs film as shown in Figure 7.

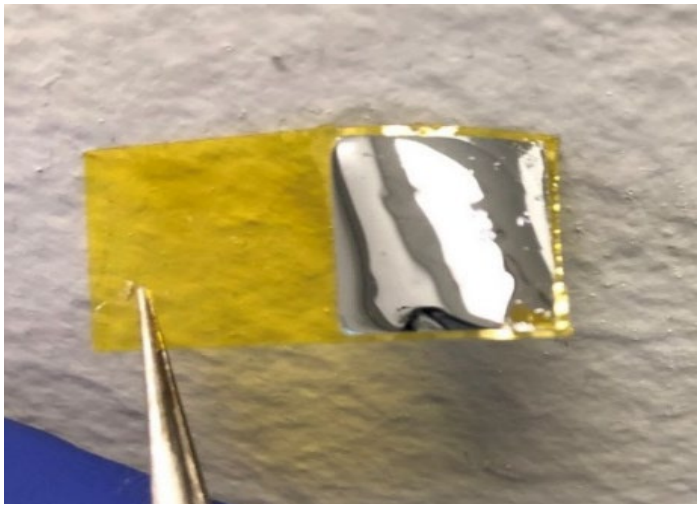

Figure 7. *GaAs/Ge/NaCl film lifted off from Ge wafer*

However, we found that Ge grown on NaCl at a lower temperature of 575°C - 600°C (needed to achieve lift off) was not epitaxial. Figure 8 shows 2D-XRD data of one such sample.

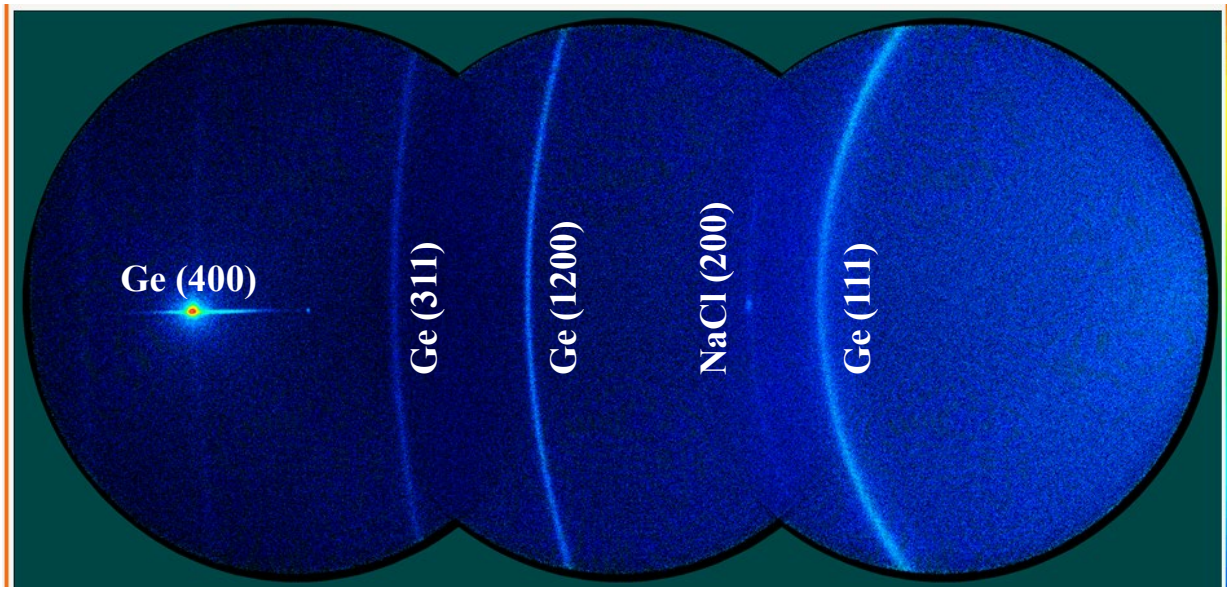

Figure 8. *2D XRD data of Ge film grown at 680°C on NaCl grown at 575°C on Ge wafer. In contrast to the case where the NaCl film is grown at 700°C, this film shows polycrystalline features.*

So, while growth of NaCl at 700°C leads to epitaxial Ge and epitaxial GaAs growth, such films could not be lifted off possibly because of desorption or degradation of NaCl. On the other hand, Ge films on NaCl grown at lower temperatures could be lifted off, but were polycrystalline.

After substantial effort to develop a NaCl-based architecture that leads to epitaxial growth and also could be lifted off, we began exploring materials alternate to NaCl that could provide the same functionality but without the issues with NaCl. Staying in the realm of halides we identified CaF_2 – BaF_2 system as our choice for NaCl-alternate. CaF_2 has been previously used as templates for epitaxial growth of Ge and GaAs films [1 - 6]. CaF_2 has a fluorite structure with a lattice parameter of 5.45Å. The solubility of BaF_2 in water is 1.7g/L. The melting temperatures of CaF_2 and BaF_2 are 1403°C and 1386 °C respectively, much higher than the melting temperature of 801 °C of NaCl. Also, the thermal expansion coefficient of CaF_2 and BaF_2 are 18.8 × 10^{-6}/°C and 18.1 × 10^{-6}/°C, substantially lower than 44 × 10^{-6}/°C of NaCl. We were able to achieve epitaxial growth of (00l) CaF_2 on GaAs substrate as shown in Figure 9.

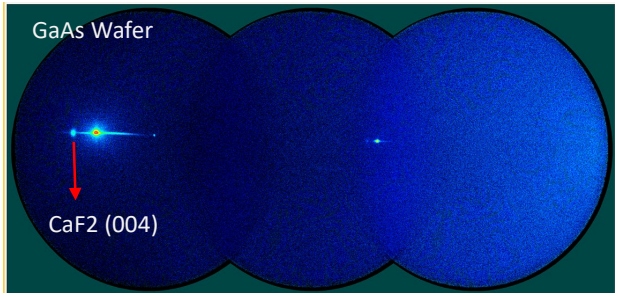

Figure 9. *2D XRD data of CaF_2 film grown on GaAs wafer. Epitaxial growth of (00l) CaF_2 is seen.*

However, it was found that the only conditions accommodating liftoff were for CaF_2 deposited at room temperature, which are porous, polycrystalline/amorphous films. Ge films deposited on epitaxial CaF_2 did not lift off. So, we introduced BaF_2 that can be used as a water-soluble sacrificial layer as its solubility in water (1.7g/L) is 2 orders of magnitude higher than CaF_2. It was however not possible to achieve (00l) epitaxial growth of BaF_2. So, we utilized a CaF_2-BaF_2-CaF_2 architecture to achieve both epitaxial growth as well as the capability for lift-off.

This architecture of epitaxial CaF_2/BaF_2/CaF_2 as possible water-soluble sacrificial buffer candidates to replace NaCl for epitaxial growth of GaAs film is shown in Figure 10. While the solubility of BaF_2 is substantially less than that of NaCl, its coefficient of thermal expansion is much lower than that of NaCl (Table I) which can be helpful in avoiding the problems we had with NaCl.

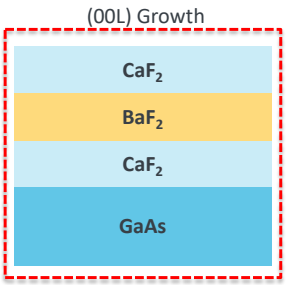

Figure 10. Schematic of *CaF_2/BaF_2/CaF_2 architecture developed for ELO of Ga-As solar cells*

Table I. *Comparison of key parameters of BaF_2 and NaCl for use as water-soluble buffers.*

Material	Lattice Constant	Solubility	CTE
GaAs/Ge	5.653/5.658	---	5.7/5.6
BaF_2	6.196	1.7 g/L	18.1
NaCl	5.65	360 g/L	44

Figure 11 displays the 2D-XRD data of BaF_2/CaF_2 films grown on GaAs wafer. As shown in the figure, both BaF_2-CaF_2 exhibited good (00l) epitaxial growth. To verify epitaxial liftoff, Ge was subsequently deposited on the BaF_2/CaF_2 architecture. We were able successfully lift off the Ge film as shown in Figure 11.

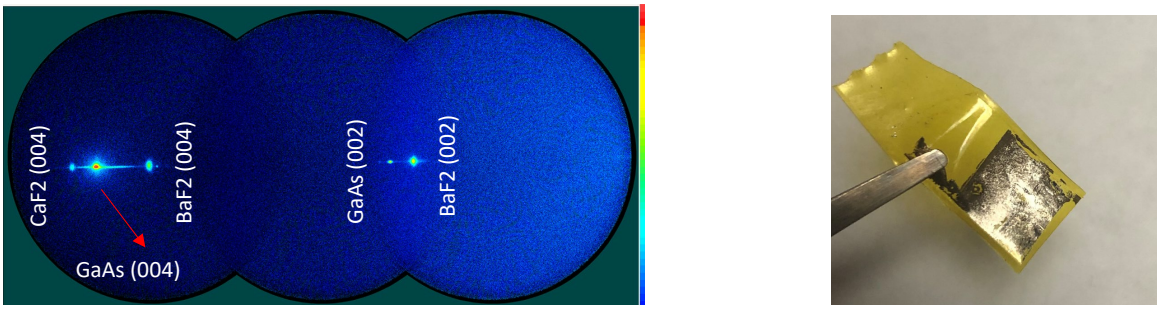

Figure 11. *(left) 2D XRD data of BaF_2/CaF_2 film grown on GaAs wafer. Epitaxial growth of (00l) CaF_2 and BaF_2 is seen. (right) Ge film grown on BaF_2/CaF_2 film on GaAs wafer after epitaxial lift off.*

For closer lattice matching with Ge and GaAs, a $CaF_2/BaF_2/CaF_2$ architecture was grown on GaAs wafer. Figure 12 shows that all 3 layers of this architecture exhibit (00l) epitaxial growth. This architecture was now used for GaAs growth as described in subtask 1.2.

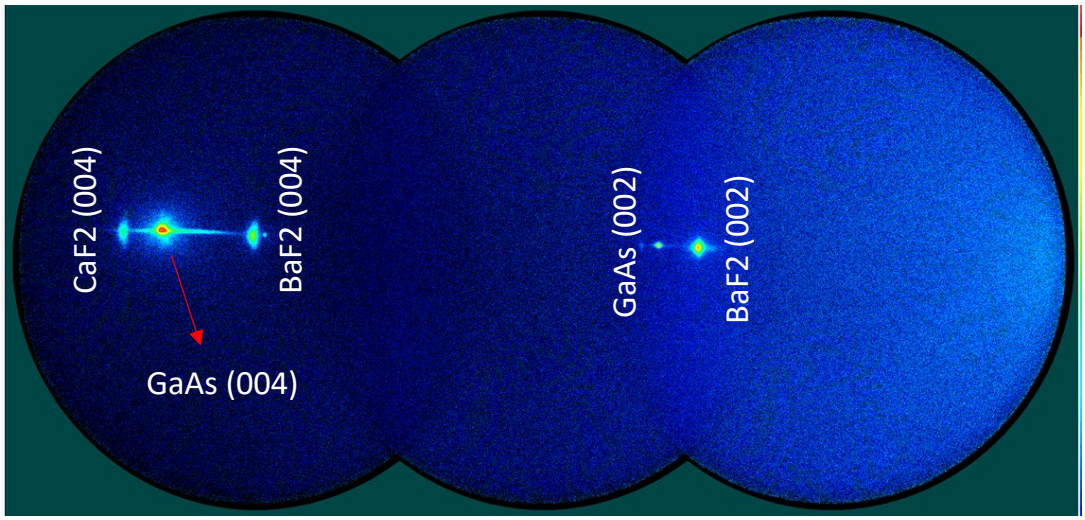

Figure 12. *2D XRD data of $CaF_2/BaF_2/CaF_2$ film grown on GaAs wafer. (00l) epitaxial growth of all 3 layers is seen.*

While epitaxial growth of GaAs was achieved with the $CaF_2/BaF_2/CaF_2$ architecture, we found that GaAs devices fabricated with this architecture exhibited polycrystallinity and twins. We believe that this was due to the lattice mismatch between CaF_2 (5.451 Å) and GaAs (5.653 Å) ~ 4%. So, we replaced CaF_2 with a two-fluoride structure (CaF_2 (5.451 Å) & SrF_2 (5.7996 Å)) engineered to match the lattice constant of GaAs. We deposited SrF_2, CaF_2, and BaF_2 by electron beam evaporation (E beam evaporation). A binary mixture of CaF_2 and SrF_2 was prepared by precisely mixing SrF_2 and CaF_2 to achieve a

lattice-matched template for GaAs. The mixture was calculated using Vegard's law and was adjusted to account for the differences in coefficients of thermal expansion (CTE) at elevated temperatures.

Figure 13 exhibits 2D-XRD data showing peak overlap of epitaxial (Sr,Ca)F_2 grown on a GaAs substrate and figure 13(right) shows the line integration of the (Sr,Ca)F_2/GaAs (004) signal where a singular peak is seen, indicating that the materials are lattice-matched.

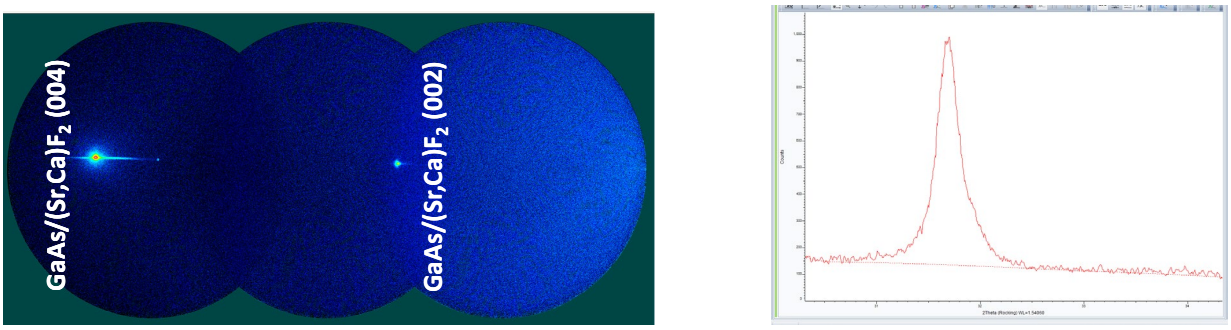

Figure 13. *2D-XRD of (Ca,Sr)F_2 epitaxially grown on GaAs wafer (Right) (004) peak of (Ca,Sr)F_2*

Epitaxial growth of BaF_2 on $(Ca_xSr_{1-x})F_2$ was done using conditions similar to BaF_2 on CaF_2. Figure 14 shows the 2D-XRD data of the epitaxially grown BaF_2 on $(Ca_xSr_{1-x})F_2$ followed by epitaxial growth of CaF_2. The lattice mismatch of BaF_2 and CaF_2 with $(Ca_xSr_{1-x})F_2$ can be seen.

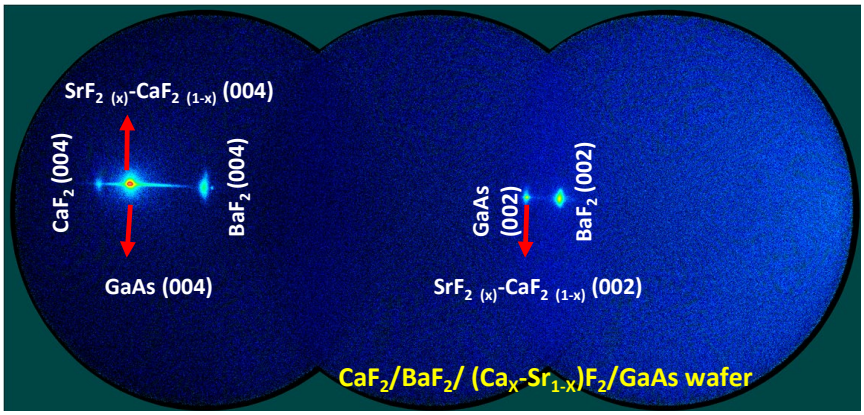

Figure 14. *2D-XRD of CaF_2/BaF_2/ $(Ca_X$-$Sr_{1-X})F_2$ epitaxially grown on GaAs wafer.*

For better lattice matching of the buffer with GaAs, a triple-layer structure $(Ca_xSr_{1-x})F_2$ /BaF_2/$(Ca_xSr_{1-x})F_2$ was fabricated. This architecture has the benefits of both lattice-matching of $(Ca_xSr_{1-x})F_2$ film with GaAs and a sacrificial water soluble BaF_2 layer. 2D-XRD data of this architecture is shown in Figure 15, revealing a good lattice matching of the top $(Ca_xSr_{1-x})F_2$ film with the GaAs wafer below. This is in spite of the lattice mismatch of BaF_2 with $(Ca_xSr_{1-x})F_2$.

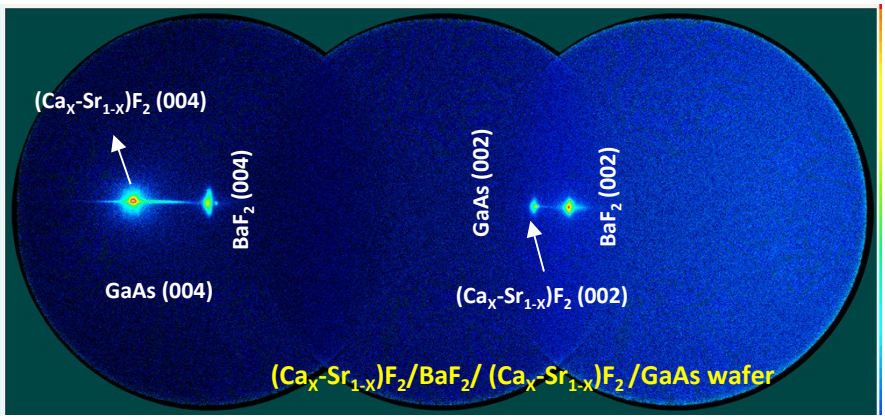

Figure 15. *2D-XRD of $(Ca_X\text{-}Sr_{1\text{-}X})F_2/BaF_2/(Ca_X\text{-}Sr_{1\text{-}X})F_2$ epitaxially grown on GaAs wafer.*

A (220) polefigure of the BaF_2 was obtained and the result is shown in Figure 16. Phi-scan extracted from the polefigure is included in the figure. The data shows a clear four-fold symmetry of BaF_2. The Full Width Half Maximum (FWHM) of integrated peaks is 1.590°.

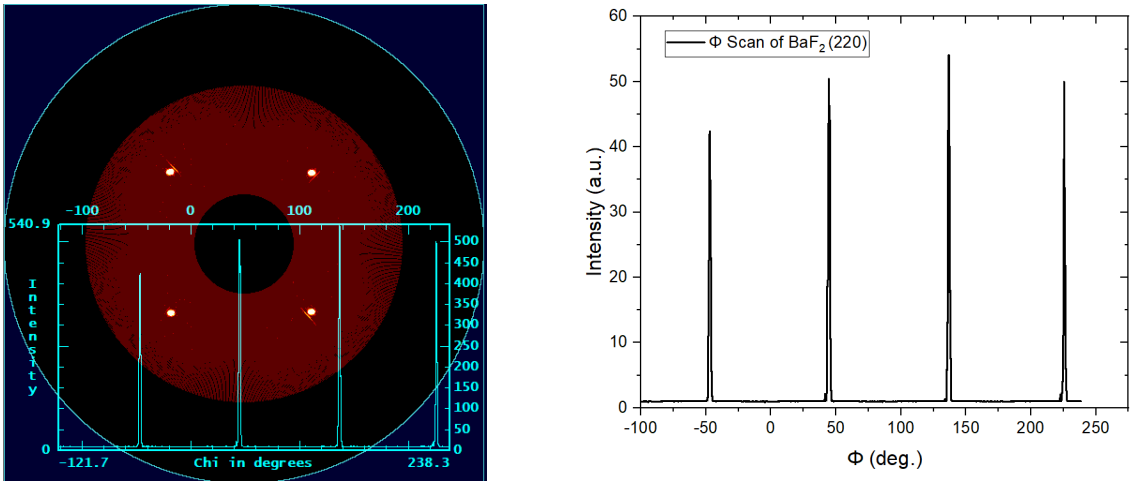

Figure 16. *(220) XRD polefigure and phi-scan of BaF_2 in $(Ca_X\text{-}Sr_{1\text{-}X})F_2/BaF_2/(Ca_X\text{-}Sr_{1\text{-}X})F_2$ buffer architecture epitaxially grown on GaAs wafer.*

As discussed in task 1.2, the $(Sr,Ca)F_2/BaF_2/(Sr,Ca)F_2$ triple layer structure led to eptiaxial growth due to its lattice matching using the lattice-engineered $(Sr,Ca)F_2$ films and easy epitaxial liftoff with a water-soluble BaF_2 film. However, defects arising from antiphase domains in the GaAs film lead to a decrease in device performance relative to a control. Thermal cyclic annealing (TCA) and the introduction of Ge, an additional lattice-matched buffer layer, were done to help reduce antiphase domain generation, which consequently should reduce the total number of defects generated in the GaAs film after MOCVD processing, ultimately improving device efficiency. Epitaxial growth of Ge film was achieved on $(Sr,Ca)F_2/BaF_2/(Sr,Ca)F_2$ triple layer structure as shown in Figure 17.

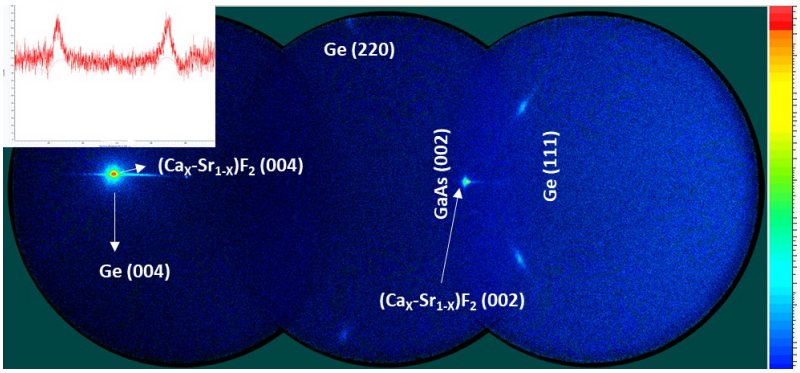

Figure 16. *2D-XRD of Ge epitaxially grown on (Ca$_X$-Sr$_{1-X}$)F$_2$/BaF$_2$/(Ca$_X$-Sr$_{1-X}$)F$_2$ buffer architecture on GaAs wafer. Inset shows integration along Ge (111) peak indicating presence of twins.*

A comparison of surface roughness of epitaxial Ge grown at different temperatures on the fluoride buffer architecture is given in Figure 17. The data reveals an improvement in surface roughness of Ge with decreasing growth temperature. Ge grown at 575°C provides a smoother surface for subsequent good GaAs growth.

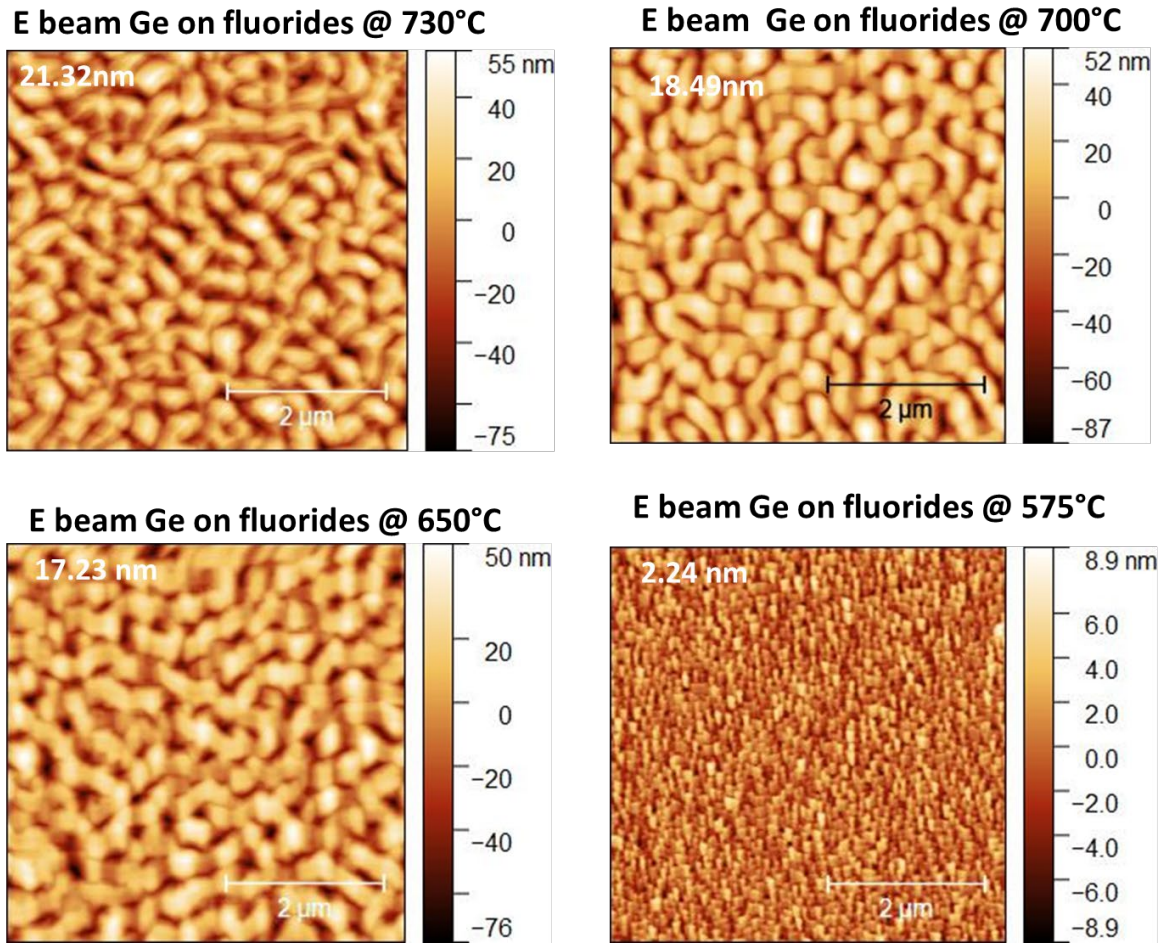

Figure 16. *Atomic Force Microscopy of Ge epitaxially grown at different temperatures on (Ca$_X$-Sr$_{1-X}$)F$_2$/BaF$_2$/(Ca$_X$-Sr$_{1-X}$)F$_2$ buffer architecture on GaAs wafer.*

Subtask 1.2: Growth and characterization of GaAs on water-soluble ELO buffer

GaAs single junction solar cell device was grown on the Ge/NaCl/GaAs wafer in our MOCVD tool. GaAs buffer layer layers were grown at 650ºC. A 1.4 µm thick highly-doped p++ GaAs layer with a bulk concentration (BC) of $5.0\times10^{19}cm^{-3}$ was grown to serve as a current-spreading layer for lateral contacts. A ~33nm p++ ($1.0\times10^{19}cm^{-3}$) back-surface field (BSF) AlGaAs layer was grown, followed by a 50 nm p-GaAs layer (1.0×10^{18} cm^{-3}) and an intrinsic GaAs layer of thickness 1000nm. The growth of the intrinsic GaAs was followed by ~67nm of n+ -type GaAs (1.0×10^{17} cm^{-3}) emitter, ~30nm of n++ ($1.0\times10^{19}cm^{-3}$) AlGaAs window layer and finally a ~33nm n++ GaAs (1.0×10^{19} cm^{-3}) cap layer to complete the p-i-n device architecture. Thickness variation in each layer is in the range of ±3nm. ToF SIMS measurements were conducted to confirm the presence of all the layers in the architecture and the results are shown in Figure 17. In addition to the GaAs and Ge layers, the presence of NaCl in the architecture is also evident.

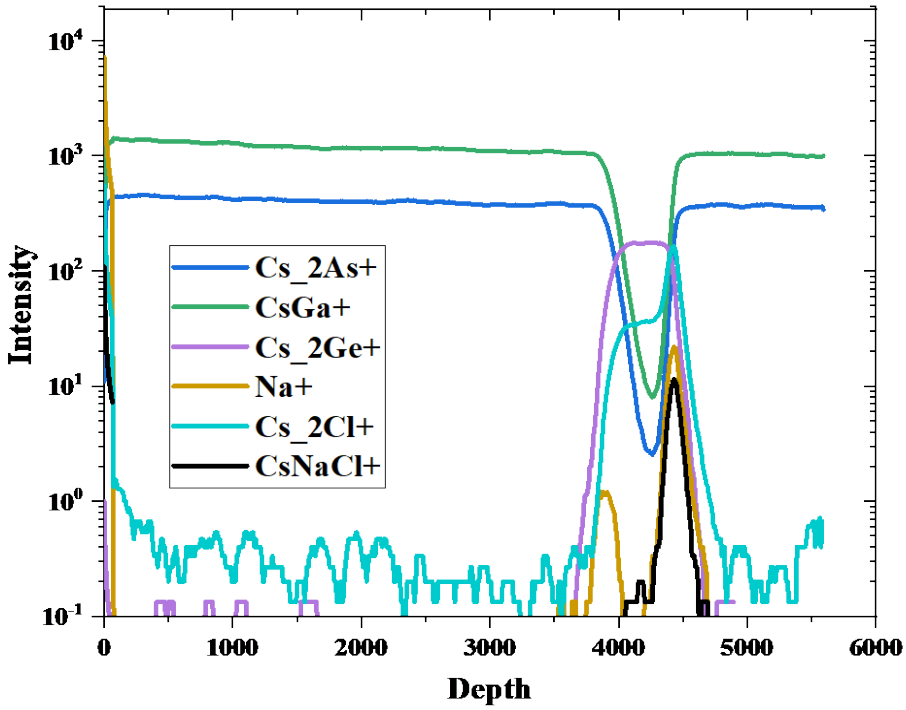

Figure 17. *TOF-SIMS data from epitaxial GaAs film grown on Ge/NaCl/GaAs wafer by MOCVD.*

Figure 18 shows Transmission Electron Microscopy (TEM) results of GaAs single junction solar cell grown on NaCl sacrificial layer structure. The the diffraction patterns from GaAs layer and cap germanium layer shown in Figure 18 (c) and (e) respectively confirm the high crystallinity of the GaAs and Ge films. Figure 18 (f) shows the presence of NaCl, but its thickness is only ~ 2 nm, much less than the 25 nm thickness observed in Figure 3 prior to GaAs growth.

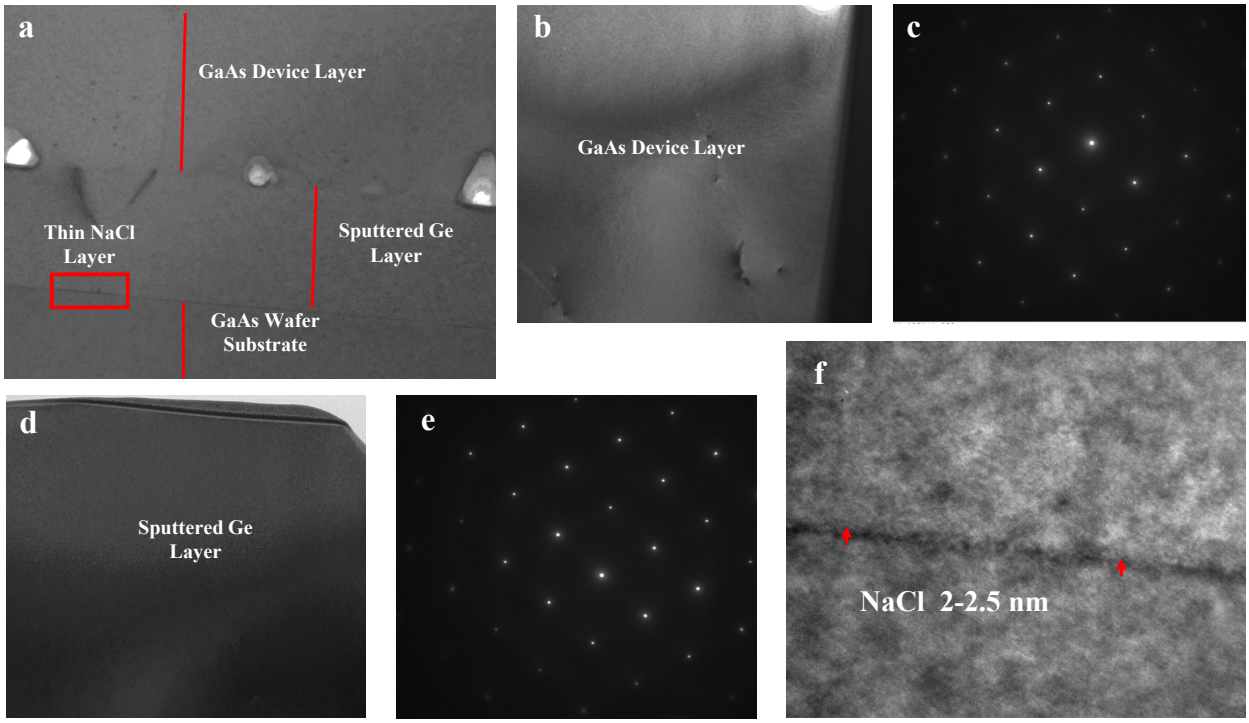

Figure 18. *Cross Sectional Transmission Electron Microscopy (TEM) images and diffraction pattern data from epitaxial GaAs film grown on Ge/NaCl/GaAs wafer by MOCVD. (a) cross-section of complete device (b)&(c) are the image and diffraction pattern of GaAs device layers. (d)&(e) are image and diffraction pattern of sputter-deposited cap layer Germanium layer (f) Interface of the GaAs wafer and sputter-deposited Ge film showing a 2.5nm thin NaCl layer.*

After we switched from NaCl to fluoride buffers, GaAs growth control runs were carried out on single layer (00*l*) CaF_2 films to explore the best GaAs growth conditions. The best quality GaAs growth were achieved using low-temperature conditions (20 Torr, 500°C), as shown on Figure 19. No non (00l) orientations of GaAs are seen confirming epitaxial growth of GaAs on CaF_2.

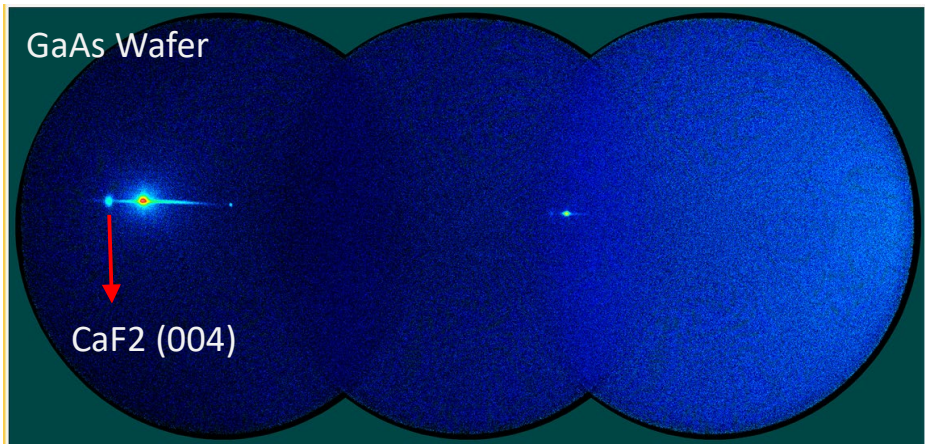

Figure 19. *2D XRD data of GaAs film grown on CaF_2 film on GaAs wafer.*

Next, GaAs was grown on $CaF_2/BaF_2/CaF_2$ architecture on GaAs wafer and 2D-XRD results are shown in Figure 20. As shown in the figure, no non (00l) orientations of GaAs are seen confirming epitaxial growth of GaAs on this tri-layer architecture.

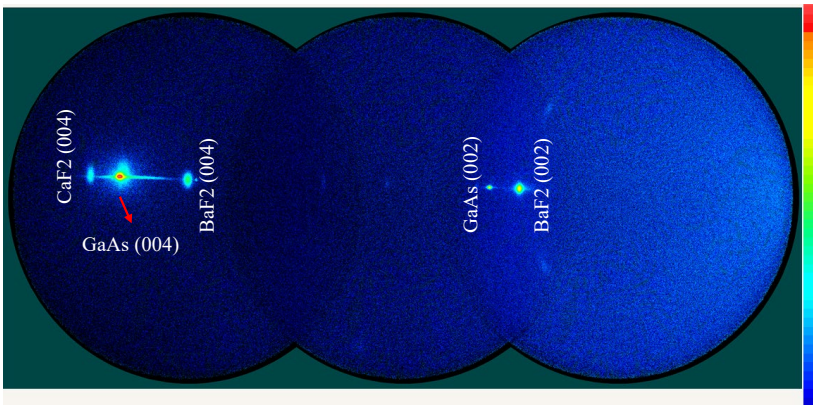

Figure 20. *2D XRD data of GaAs film grown on $CaF_2/BaF_2/CaF_2$ architecture on GaAs wafer.*

Cross-sectional TEM micrograph of a GaAs film grown at a higher temperature up to 650º on $CaF_2/BaF_2/CaF_2$ architecture on GaAs wafer is shown in Figure 21. As shown in the figure, the thickness of the CaF_2 and BaF_2 layers are seen to be 110 – 140 nm. Some polycrystallinity and twins are observed in the GaAs film which must be due to higher temperature used for its growth. Selected area diffraction pattern of the GaAs wafer - $CaF_2/BaF_2/CaF_2$ layers is included in Figure 21 and reveal the presence of all layers after GaAs growth.

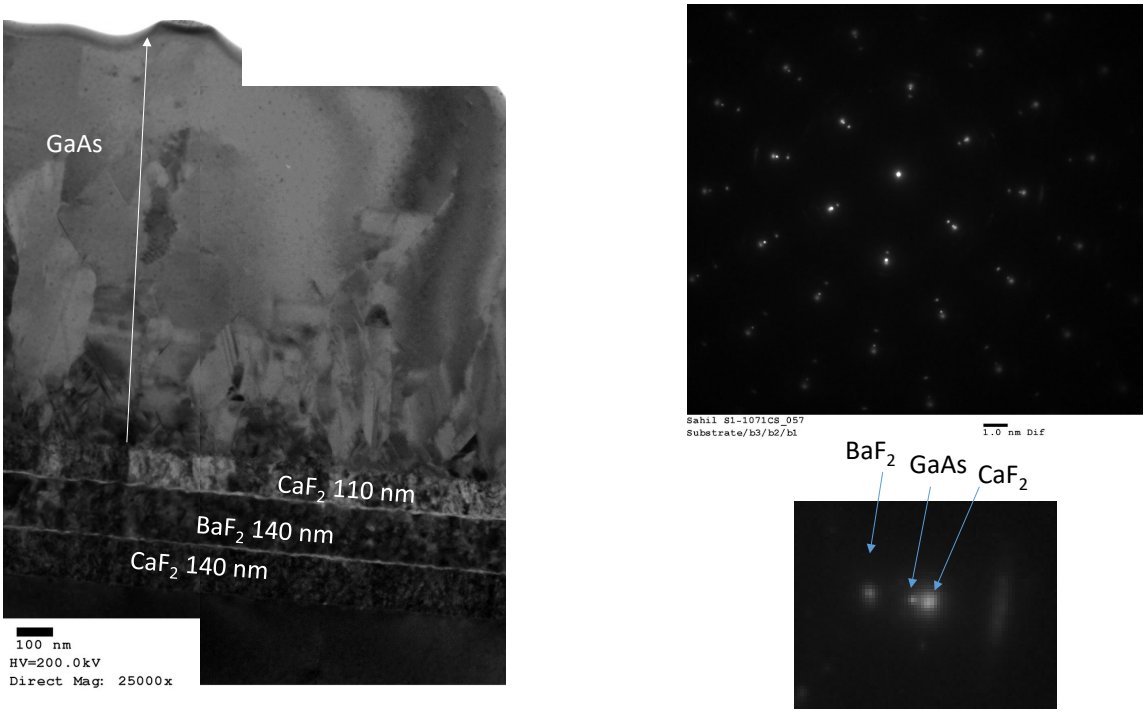

Figure 21. *(Left) Cross-sectional TEM micrograph of a GaAs film grown on $CaF_2/BaF_2/CaF_2$ architecture on GaAs wafer. (right) selected area diffraction pattern of GaAs wafer - $CaF_2/BaF_2/CaF_2$ layers.*

Next GaAs was epitaxially grown by MOCVD on the $(Ca_xSr_{1-x})F_2$-capped film. TEM diffraction analysis (Figure 22) shows epitaxial growth of the GaAs film on $(Ca_xSr_{1-x})F_2$. As seen in Figure 22, GaAs film grown on the lattice-matched triple-layer $(Ca_xSr_{1-x})F_2$ /BaF_2/$(Ca_xSr_{1-x})F_2$ architecture exhibits less defects compared with GaAs grown on $(Ca_xSr_{1-x})F_2$ /BaF_2/CaF_2 architecture.

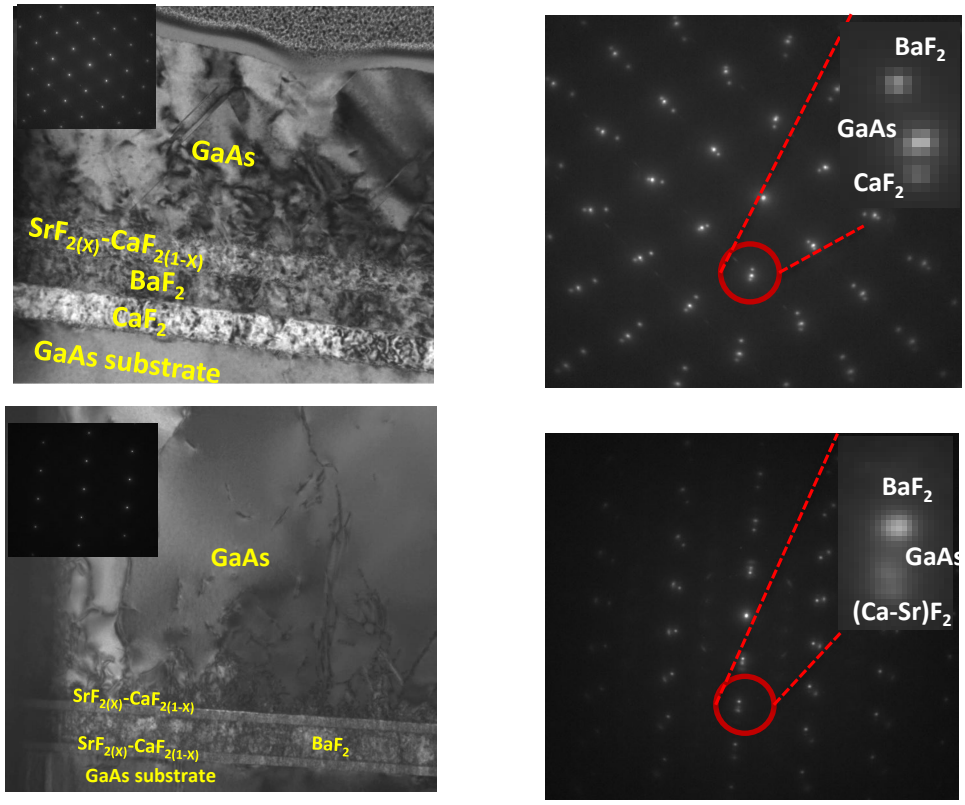

Figure 22. *Cross sectional TEM and diffraction patterns of GaAs film grown on $(Ca_X\text{-}Sr_{1-X})F_2/BaF_2/CaF_2$ (above) and on $(Ca_X\text{-}Sr_{1-X})F_2/BaF_2/(Ca_X\text{-}Sr_{1-X})F_2$ buffer architectures on GaAs wafer.*

Time-of-Flight Secondary Ion Mass Spectrometry (ToF-SIMS) analysis was conducted on the GaAs film grown on $(Ca_xSr_{1-x})F_2$ /BaF_2/$(Ca_xSr_{1-x})F_2$ architecture and the result in shown in Figure 23. The data shows that metallic ion diffusion from buffer to the GaAs film is negligible, confirming the stability of fluoride buffer during high temperature GaAs process.

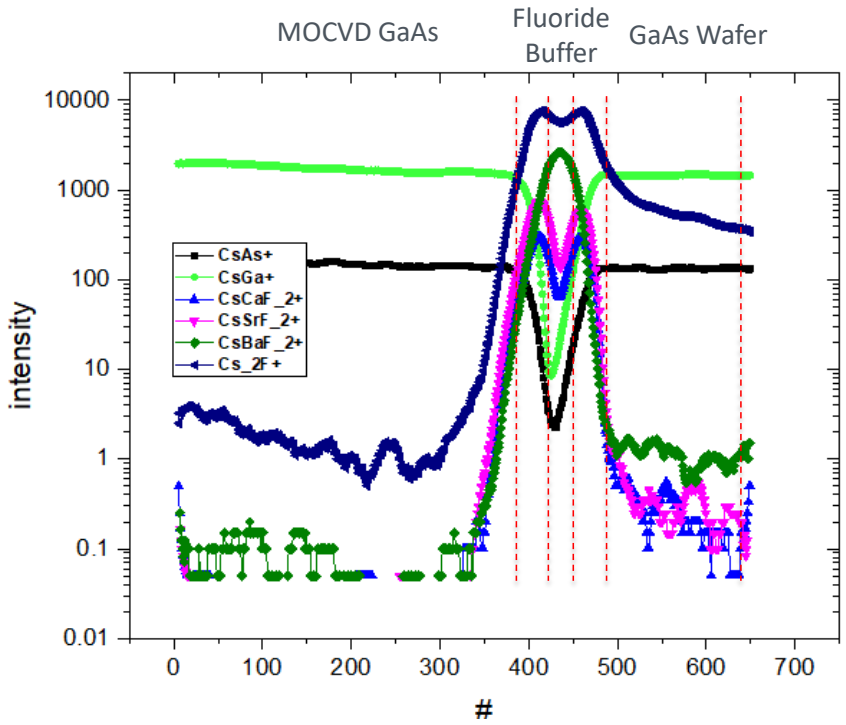

Figure 23. *TOF-SIMS analysis of GaAs film grown on $(Ca_X\text{-}Sr_{1\text{-}X})F_2/BaF_2/(Ca_X\text{-}Sr_{1\text{-}X})F_2$ buffer architecture on GaAs wafer.*

Thermal cyclic annealing (TCA) is a proven technique that has been demonstrated to reduce threading dislocations in lattice-mismatched films such as GaAs on Si. Although the defects in our case with fluoride buffers are not necessarily due to lattice mismatch, but arise from antiphase domains, the same approach was taken to annihilate these defects. A GaAs film of about 500nm was grown on the fluoride template, then cooled to 300°C, followed by heating the sample to 700°C, and annealing the sample at the elevated temperature for 1 minute before cooling to 300°C. This constitutes 1 TCA cycle. A total of 5 TCA cycles were done before continuing GaAs growth at the standard optimized conditions (20 Torr, 650°C) to prepare the sample for a device growth.

As mentioned in section 1.1, Ge was grown on the group II fluoride buffer to facilitate epitaxial growth of Ge. The optimal conditions for GaAs grown on any of the Ge samples grown on (00l) were the same as our standard conditions for GaAs on fluorides. 2D XRD of the GaAs films showed good epitaxy and microscopy revealed smooth films (Figure 24).

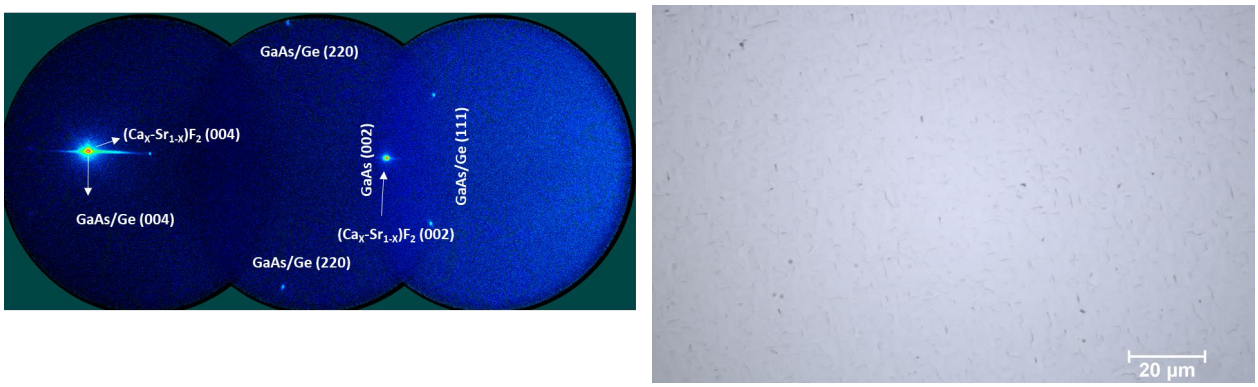

Figure 24. *2D XRD (left) and SEM image (right) of GaAs film grown on Ge on (Ca$_X$-Sr$_{1-X}$)F$_2$/BaF$_2$/(Ca$_X$-Sr$_{1-X}$)F$_2$ buffer architecture on GaAs wafer.*

Subtask 1.3: Fabrication and testing of single-junction GaAs solar cells

Initially, solar cell devices were fabricated on the GaAs/Ge/NaCl architecture. A circular mesa design was patterned by lithography and etched down to the highly-doped p-GaAs layer to make the bottom contact, using a GaAs etchant. After the mesa structure, metal contacts for p-type bottom and n-type top contacts were deposited and patterned using electron-beam evaporation and lift-off technique. Au/Ge/Ni was used for n-ohmic contact and for the p-ohmic contact, Au/Ti was used. Contact resistance and sheet resistance of both p-type GaAs and n-type GaAs were both measured using Transmission Line Method. The completed devices were measured using a AAA solar simulator, simulating a AM1.5G spectrum at an intensity of 1 sun. Data from a single GaAs solar cell on a structure consisting of NaCl layer as described in Figures 12 and 13 revealed a diode behavior with significant kick-in voltage. I-V measurements of two identical devices under illumination are shown in Figure 25. An open circuit voltage of devices 1 & 2 was 767 and 759 mV respectively. The conversion efficiency was recorded to be 11.04% and 10.43% for devices 1 & 2 respectively. Unfortunately, these solar cell devices did not lift off possibly because of the very thin layer of NaCl left after GaAs growth.

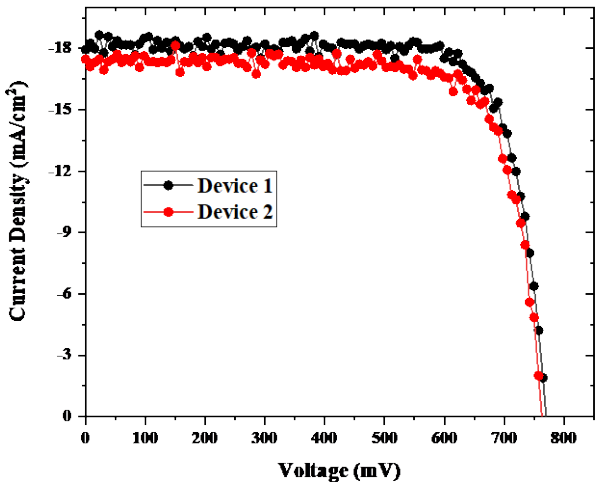

Figure 25. *Illuminated J-V plot of GaAs solar cell using NaCl sacrificial layer before lift off.*

As described in Task 1.1, we shifted our effort from using a NaCl sacrificial layer because of the conflicting demands of low-temperature growth for lift off and high-temperature growth for epitaxy of subsequently-grown Ge. We worked on fabrication of solar cell devices using GaAs grown on $CaF_2/BaF_2/CaF_2$ architecture. A p-i-n solar cell architecture similar to that described earlier for a GaAs/Ge/NaCl structure was used. The only difference was growth of GaAs buffer layer at 500°C. The structure of the P-I-N solar cell device is shown in Table II. The solar cell devices were fabricated using the lithography method and contacts material described earlier for GaAs/Ge/NaCl structure.

Table II. *P-I-N GaAs solar cell device structure on GaAs/$(Ca_X\text{-}Sr_{1\text{-}X})F_2/BaF_2/(Ca_X\text{-}Sr_{1\text{-}X})F_2$ /GaAs wafer*

Layer	Thickness
N++ (GaAs:Si)	33nm
N++ (AlGaAs:Si)	33nm
N+ (GaAs:Si)	67nm
I (GaAs)	1000nm
P+ (GaAs:Zn)	100nm
P++ (AlGaAs:Zn)	33nm
P++ (GaAs:Zn)	1500nm

2D-XRD data of the device (Figure 26) showed presence of a few of micro-twins in GaAs film. A 1 µm GaAs buffer was deposited on the fluoride buffer to reduce stress induction in GaAs active layers (Figure 26).

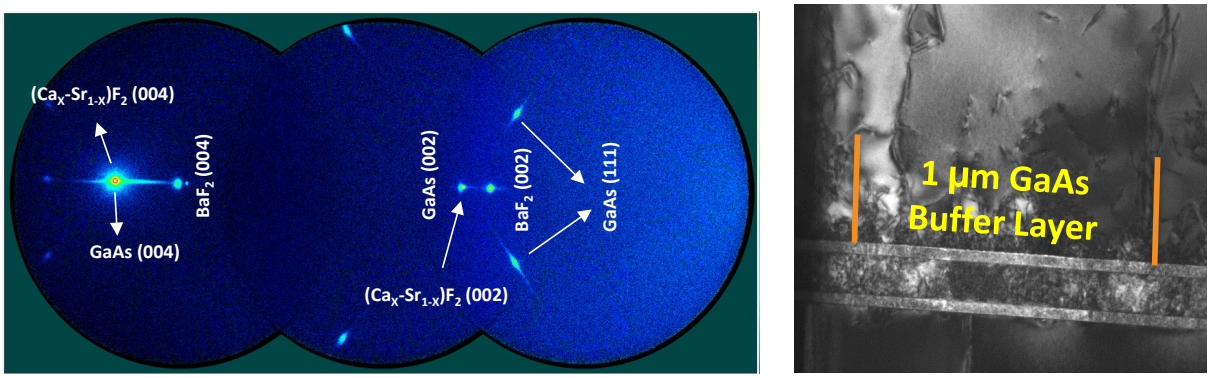

Figure 26. *2D-XRD (left) and cross-sectional TEM of P-I-N device fabricated on GaAs film grown on $(Ca_X\text{-}Sr_{1\text{-}X})F_2/BaF_2/(Ca_X\text{-}Sr_{1\text{-}X})F_2$ buffer architecture on GaAs wafer.*

Contact resistance and sheet resistance of both p-type GaAs and n-type GaAs were both measured using Transmission Line Method. The solar cells showed low contact resistance and sheet resistance (Figure 27).

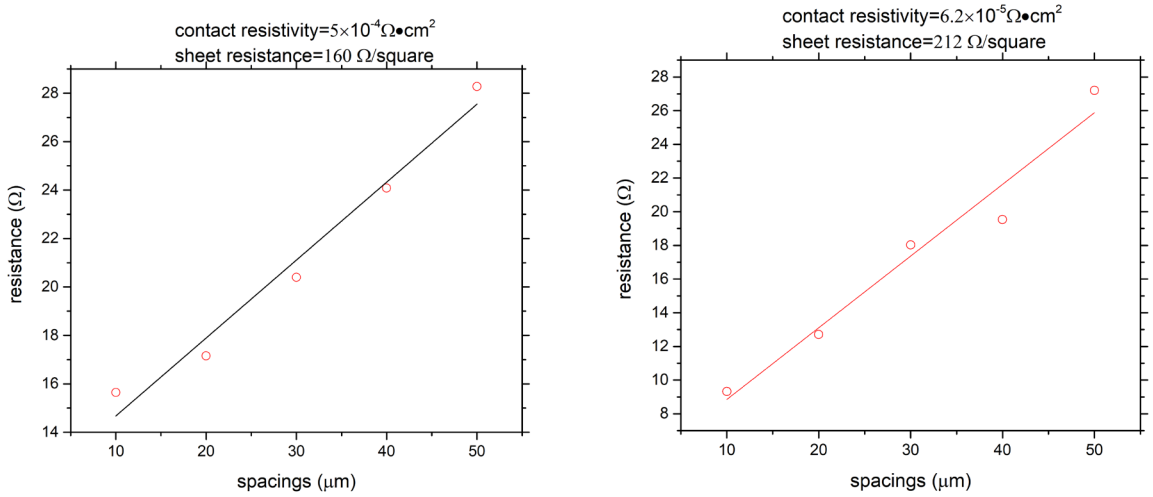

Figure 27. *Top TLM (left) and bottom TLM (right) data from contact resistivity measurements on P-I-N device fabricated on GaAs film grown on $(Ca_X\text{-}Sr_{1\text{-}X})F_2/BaF_2/(Ca_X\text{-}Sr_{1\text{-}X})F_2$ buffer architecture on GaAs wafer.*

Figure 28 exhibits dark-current measurement from the P-I-N solar cell and no significant leakage current is observed.

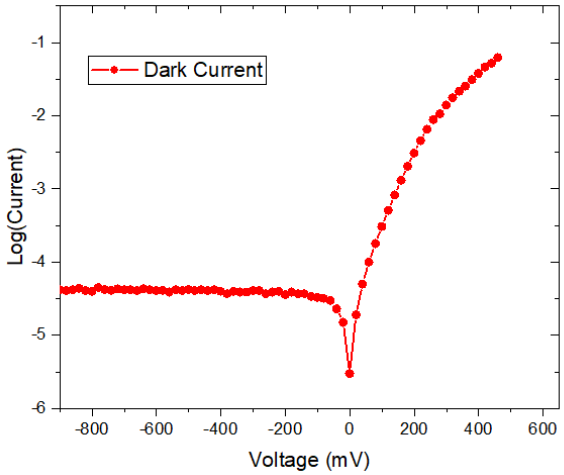

Figure 28. *Dark current measurement of P-I-N device on GaAs/$(Ca_X\text{-}Sr_{1\text{-}X})F_2/BaF_2/(Ca_X\text{-}Sr_{1\text{-}X})F_2$ buffer architecture on GaAs wafer.*

The completed devices were measured using a AAA solar simulator, simulating a AM1.5G spectrum at an intensity of 1 sun. I-V curves before and after cap layer removal of three different solar cells made on the water-soluble ELO buffer is shown Figure 29. The solar cell parameters are included in the tables below the figures.

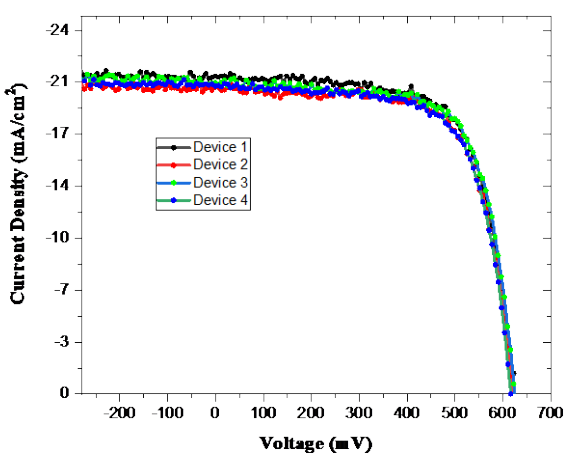

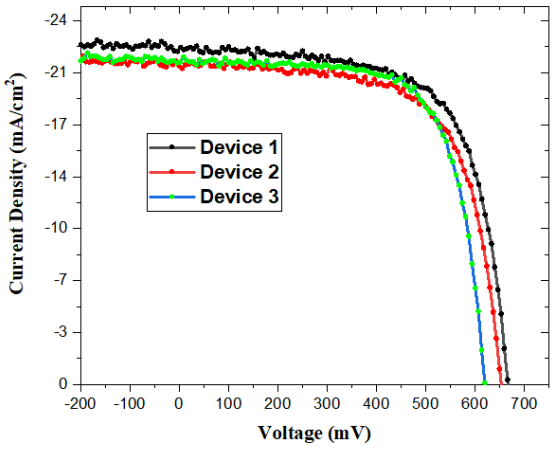

Device	V_{OC} (mV)	I_{SC} (mA/cm²)	FF (%)	Eff (%)
1	621	20.69	71	9.13
2	619	20.29	70	8.80
3	619	21.06	70	9.12

Device	V_{OC} (mV)	I_{SC} (mA/cm²)	FF (%)	Eff (%)
1	665	22.15	75	11.05
2	653	21.45	74	10.36
3	622	21.86	74	10.05

Figure 29. *Illuminated I-V curves before (left) and after (right) cap layer removal from P-I-N device on GaAs/(Ca_X-Sr_{1-X})F_2/BaF_2/(Ca_X-Sr_{1-X})F_2 buffer architecture on GaAs wafer.*

It can be seen from Figure 29 that open circuit voltage levels above 600 mV, short circuit current density levels above 21 mA/cm^2 and fill factor of about 75% have been achieved in the GaAs solar cells on the triple-layer ELO buffer. Consequently, a conversion efficiency of 10 – 11% has been attained.

Task 2.0: Optimization of ELO process with water-soluble sacrificial buffer

The thickness of the BaF_2 sacrificial layer was optimized for ELO in water. It was found a minimum thickness of 50 nm was needed for ELO. We developed a wax-based ELO process and transferred the solar cell after lift-off to Kapton tape. Solar cell measurements were done at AMG1.5 condition as before and the results are shown in Figure 30. As shown in the figure, the devices showed less than 2% degradation in conversion efficiency after lift-off and transfer.

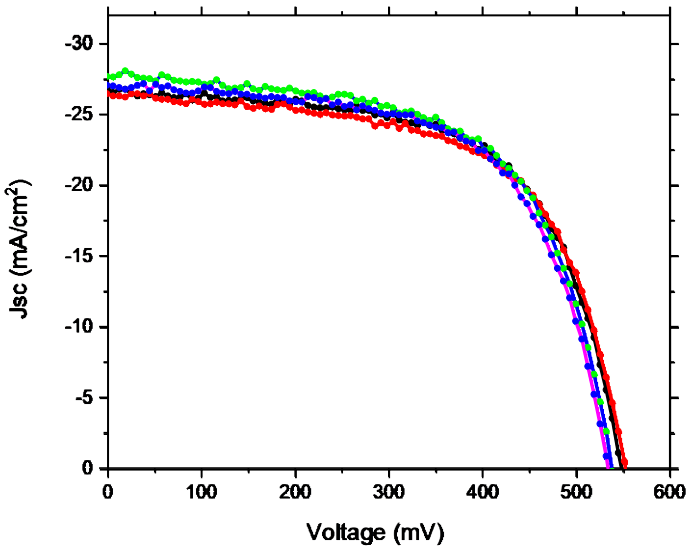

Category	Sample	V_{oc} (mV)	Jsc (mA/cm²)	FF	Efficiency (%)
Before ELO	A	547.6	27.13	0.634	10.61
After ELO		543.4	26.76	0.633	10.39
Before ELO	B	556.3	26.92	0.651	9.75
After ELO		552.4	27.02	0.650	9.71
Before ELO	C	551.7	27.51	0.653	9.91
After ELO		547.3	27.16	0.650	9.73

Figure 30. *Illuminated I-V curves of 3 solar cells before and after ELO and transfer to Kapton.*

Task 3.0: Regrowth and fabrication of GaAs solar cells after ELO without CMP

Post lift off, GaAs wafer had a (Ca-Sr)F_2 terminated film. So, the (Ca-Sr)F_2 film was washed off with very dilute HCl : water (1:20) solution within few seconds. A clean, untreated GaAs wafer was retrieved and prepared to remove native oxide for buffer deposition. The first buffer of $Ca_xSr_{1-x}F_2$ was successfully regrown epitaxially on the wafer as shown in Figure 31 (left). Next, the extended architecture of $(Ca_xSr_{1-x})F_2$ /BaF_2/$(Ca_xSr_{1-x})F_2$ was also re-grown epitaxially on the wafer– Figure 31 (right).

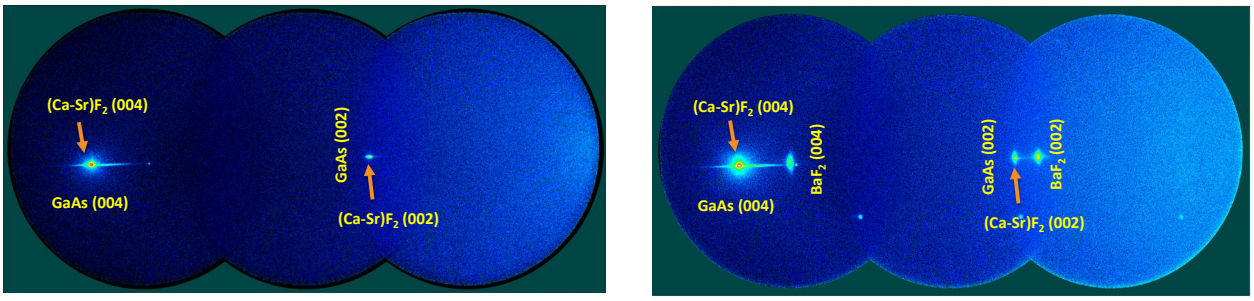

Figure 31. *2D-XRD of $Ca_xSr_{1-x}F_2$ (left) and $(Ca_xSr_{1-x})F_2$ /BaF_2/$(Ca_xSr_{1-x})F_2$ (right) re-grown on GaAs wafer after ELO.*

GaAs was successfully grown epitaxially on the fluoride buffers on the re-used wafer, as shown in Figure 32. Presence on GaAs twins was seen.

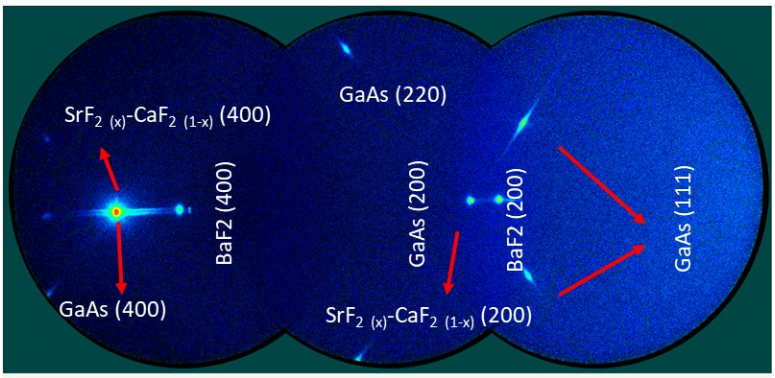

Figure 31. *2D-XRD of GaAs grown on $(Ca_xSr_{1-x})F_2$ /BaF_2/$(Ca_xSr_{1-x})F_2$ re-grown on GaAs wafer after ELO.*

Single junction GaAs device was grown and fabricated on re-grown buffer on reused wafer. A low roughness of GaAs surface was observed in re-grown sample. As shown in Figure 32, a conversion efficiency of 10.2% achieved on re-grown device indicating no loss in performance by re-use of the wafer without CMP.

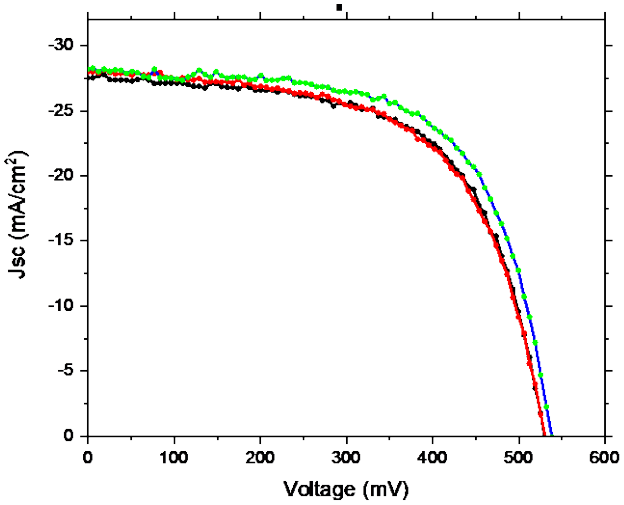

Growth	V_{oc} (mV)	Jsc (mA/cm²)	FF	Efficiency (%)
1	557.3	28.2	0.66	10.31
2 - reused wafer	551.7	28.3	0.65	10.21

Figure 32. *Illuminated I-V curves and solar cell parameters of single junction GaAs solar cells fabricated with fluoride buffer architecture, on virgin wafer and re-used wafer without CMP after ELO.*

The solar cell device described in Figure 32 was lifted off by ELO process described earlier and the wafer was reused for the second time for a third time buffer and GaAs growth. ELO buffer regrown on twice reused wafer was epitaxial as shown in Figure 33

(left). GaAs on the ELO buffer on the twice reused wafer was smooth and epitaxial with twin orientations as shown in Figure 33 (right).

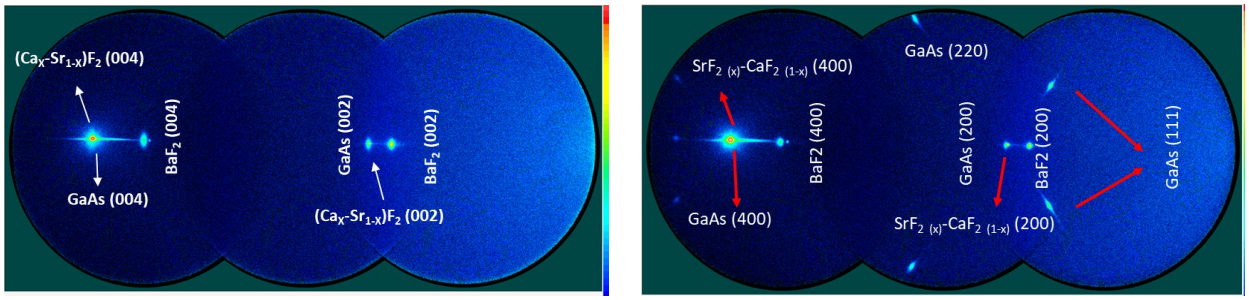

Figure 33. *2D-XRD of $(Ca_xSr_{1-x})F_2$ /BaF_2/$(Ca_xSr_{1-x})F_2$ (left) and GaAs (right) grown for the third time on twice re-used GaAs wafer after ELO.*

Single junction GaAs device was grown and fabricated on re-grown buffer on twice re-used wafer after ELO without CMP. As shown in Figure 34, a conversion efficiency of 10.4% achieved on twice re-grown device confirming *no loss in performance!*

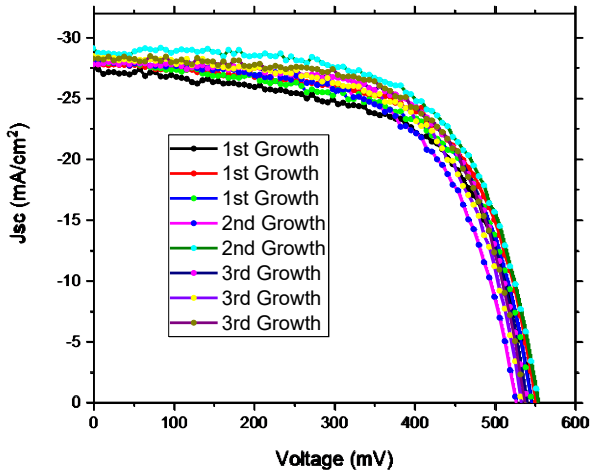

Growth	V_{oc} (mV)	Jsc (mA/cm^2)	FF	Efficiency (%)
1	557.3	28.2	0.66	10.31
2 - reused wafer	551.7	28.3	0.65	10.21
3 - reused wafer	536.3	27.9	0.69	10.39

Figure 34. *Illuminated I-V curves and solar cell parameters of single junction GaAs solar cells fabricated with fluoride buffer architecture, on virgin wafer, re-used wafer, and twice re-used wafer without CMP after ELO.*

Task 4.0: Improvement of conversion efficiency of GaAs solar cells with ELO architecture

We began this task with P-I-N solar cell device fabricated on GaAs wafer. An as-fabricated single junction P-I-N GaAs solar device showed a power conversion efficiency of 16%. To further improve the device performance and minimize reflectance loss, cap layer removal and anti-reflection coating were done. Double layer antireflection coatings composed of zinc sulfide (ZnS) and magnesium fluoride (MgF_2) were used. The thicknesses of ZnS (48nm) and MgF_2 (104nm) were optimized on a GaAs device to achieve minimum reflectance at 1 sun reference spectrum. A reflectance versus wavelength graph for the optimized ZnS and MgF_2 coatings showed reflectance less than 5% (Figure 35).

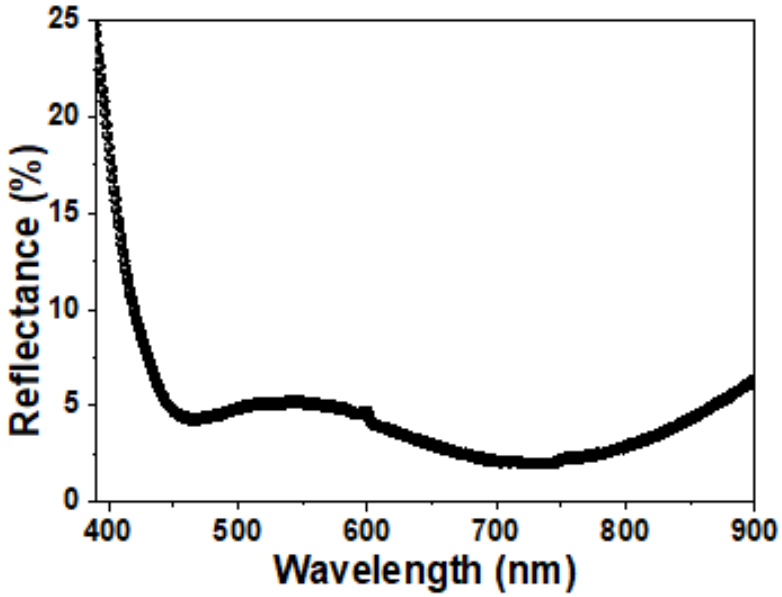

Figure 35. *Double layer ARC reflectance for optimized ZnS (48nm)/MgF_2(104nm) on reference GaAs solar cell.*

Devices characterized post ARC at 1 sun showed a significant increase in current density and further improved the power conversion efficiency up to 20% and beyond. Figure 36 shows the I-V curves of antireflection-coated single junction GaAs solar cells. The solar cells show a conversion efficiency of 20%.

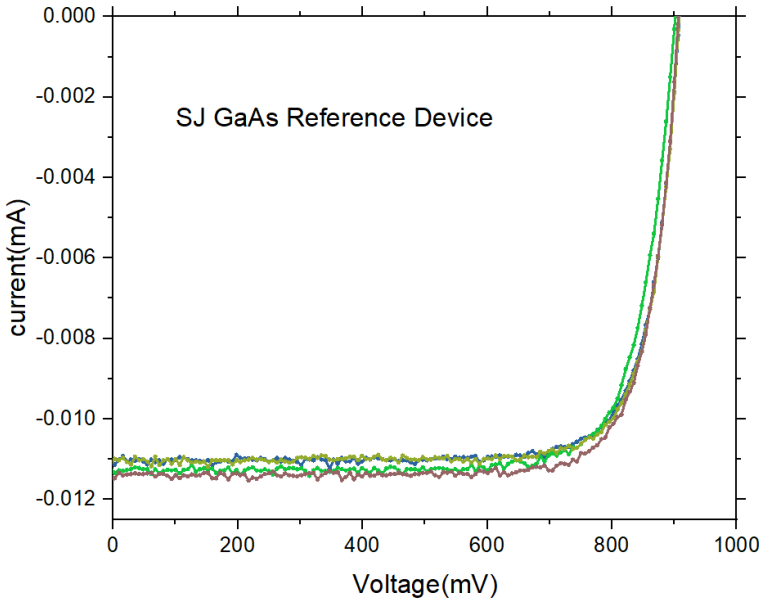

Voc (mV)	Jsc (mA/cm²)	F.F. (%)	Eff. (%)
855	29.07	80	20.04
855	29.22	79	19.84
834	29.84	78	19.53
853	29.14	80	20.04

Figure 36. *Illuminated I-V curves of four reference GaAs solar cells on GaAs wafer after ARC. Key PV parameters are shown in the table below.*

In addition to ARC, we worked to improve the efficiency of solar cells on ELO architecture by reducing the defect density. One type of defect is antiphase domains in the GaAs film when grown on the triple-layer fluoride structure. We worked on this issue by employing a vicinal GaAs substrate to overcome the mismatch in symmetry of bonding configuration of GaAs and fluorides. As shown in the schematic in Figure 37 (left), the 15º misorientation towards to (511) direction leads to a stepped surface, where terraces are on (100) plane and steps lie along the [0-1-1] direction and compensate for the angular deviation between (100) and (511) planes. These characteristics lead to two-fold symmetry and serves as a template for improved surface ordering, thereby deterring the formation of antiphase domains. Figure 37 (right) shows the 2D-XRD of a bare GaAs (511)B wafer substrate. The measurement was done in a way to extract information from both (00L) and (m11) zone axes.

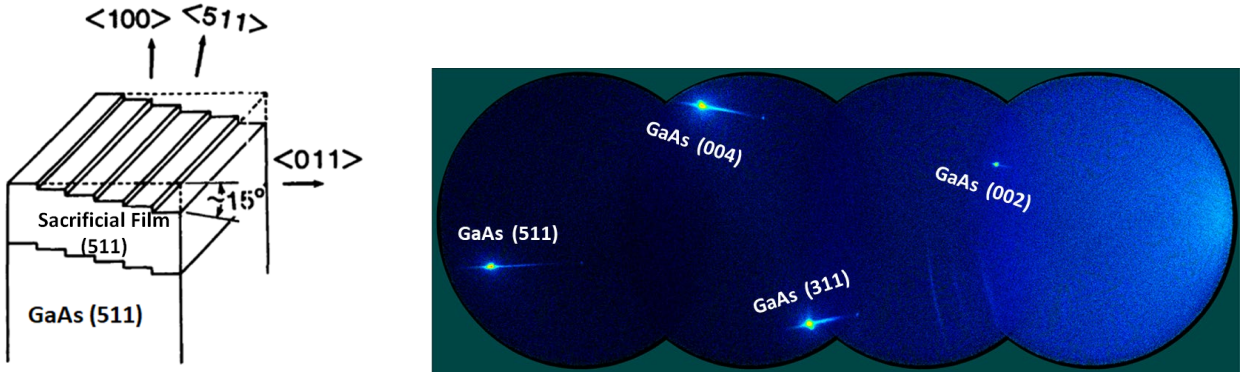

Figure 37. *(Left) Schematic of (511) GaAs substrate showing vicinal orientation of (100) planes. (Right) 2D-XRD data from a (511) GaAs wafer.*

SrF_2 was subsequently deposited on the (511) substrate to determine whether this new substrate can serve as a template for epitaxial growth of four-fold symmetric group II-fluorides. Figure 38 shows a highly textured, epitaxial SrF_2 deposited on the vicinal substrate. Once epitaxial growth is demonstrated to be possible on the template, the complete $(Sr,Ca)F_2/BaF_2/(Sr,Ca)F_2$ triple layer structure was grown on the vicinal substrate and the 2D-XRD from this architecture is shown in Figure 39. As seen on the figure, the film is epitaxial and highly textured, analogous to a similar structure grown on a (00l) wafer. This architecture was next used for GaAs device fabrication.

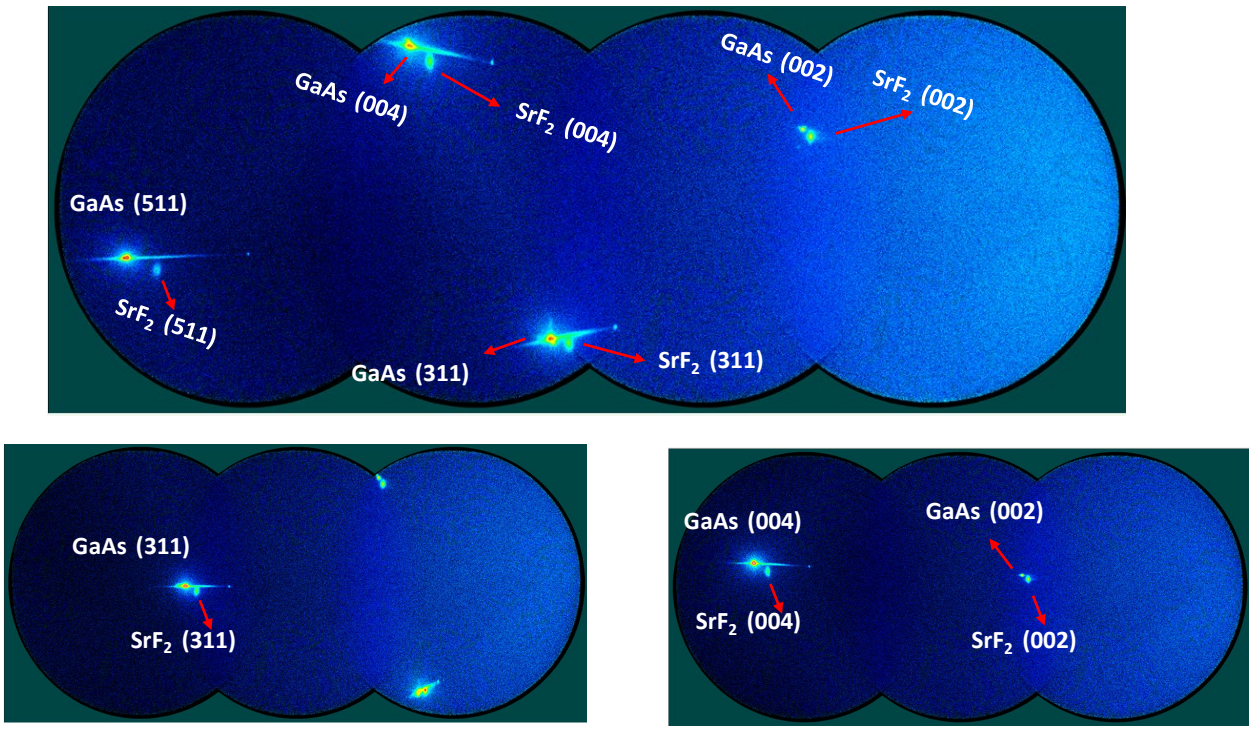

Figure 38. *2D-XRD data showing epitaxial growth of SrF_2 on (511) GaAs wafer.*

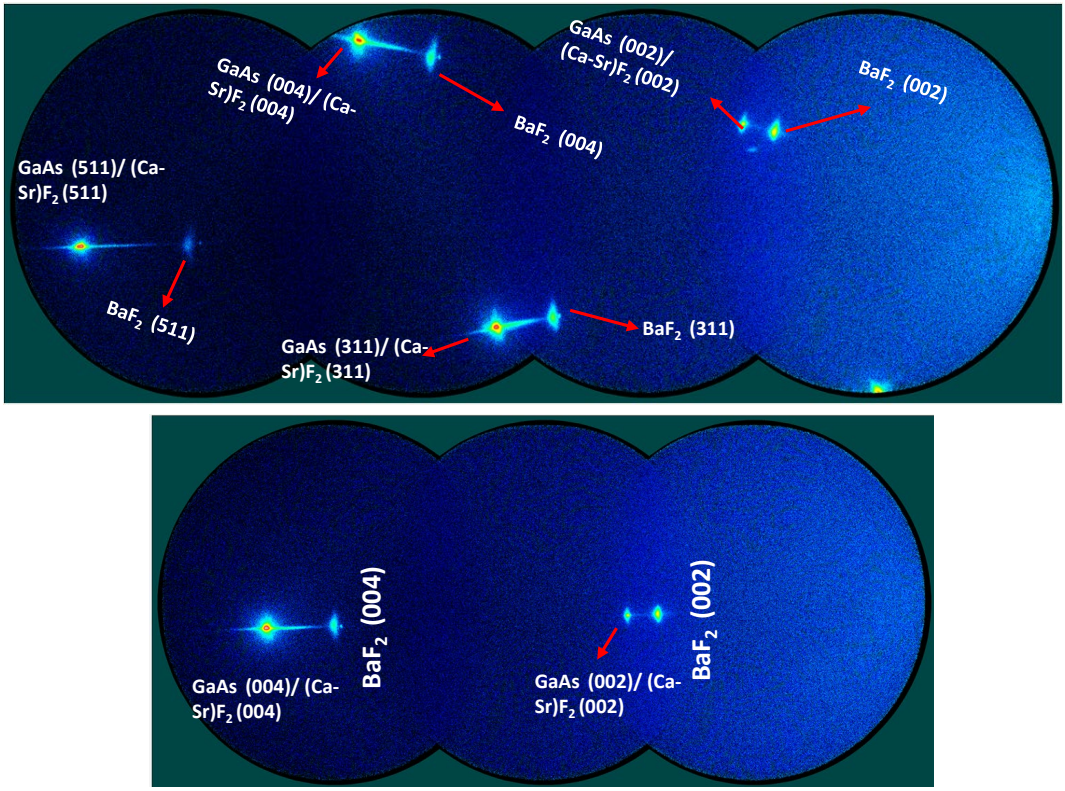

Figure 39. *2D-XRD data showing epitaxial growth of $(Ca_X\text{-}Sr_{1\text{-}X})F_2/BaF_2/(Ca_X\text{-}Sr_{1\text{-}X})F_2$ buffer architecture on (511) GaAs wafer.*

Figure 40 shows the comparison of the fluoride buffer microstructure grown on standard GaAs (00L) substrate, and on GaAs (511B) vicinal substrate. Clearly, buffer deposited on GaAs (511B) substrate showed growth along the steps resulting in elongated grains compared to pyramidal shaped grains observed for buffer grown on standard GaAs (00L) substrate. The nucleation alkaline earth compounds along steps of vicinal substrate eliminates the growth of anti-phase domains of GaAs which acts as non-radiative recombination centers.

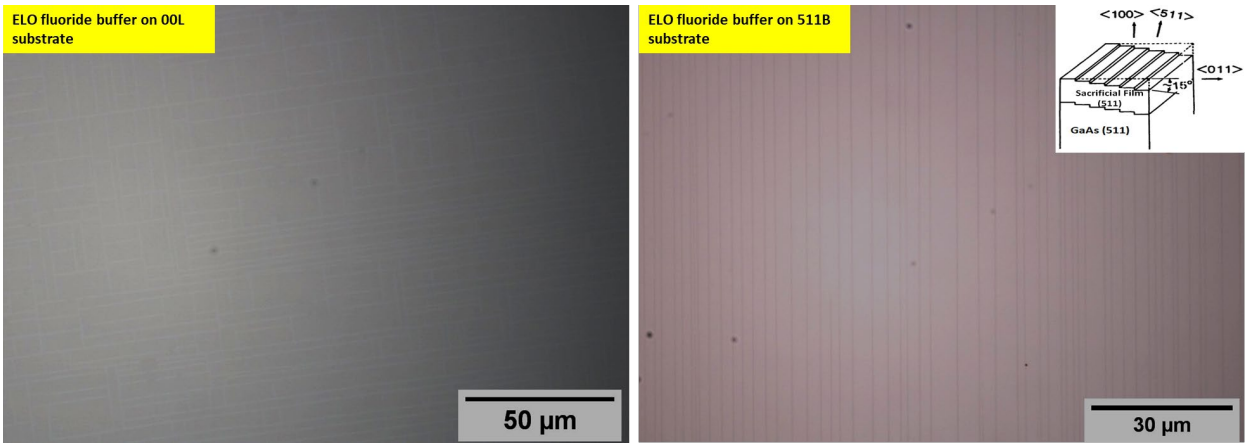

Figure 40. *Optical micrographs of $(Ca_X\text{-}Sr_{1\text{-}X})F_2/BaF_2/(Ca_X\text{-}Sr_{1\text{-}X})F_2$ buffer architecture on (00l) GaAs wafer (left) and on (511) GaAs wafer (right).*

Figure 41 shows the highly textured Ge film grown on the fluoride structure on vicinal GaAs substrate (GaAs (511)) at two different temperatures. The optimal deposition conditions for this substrate were found to be the same as on (00l) substrates.

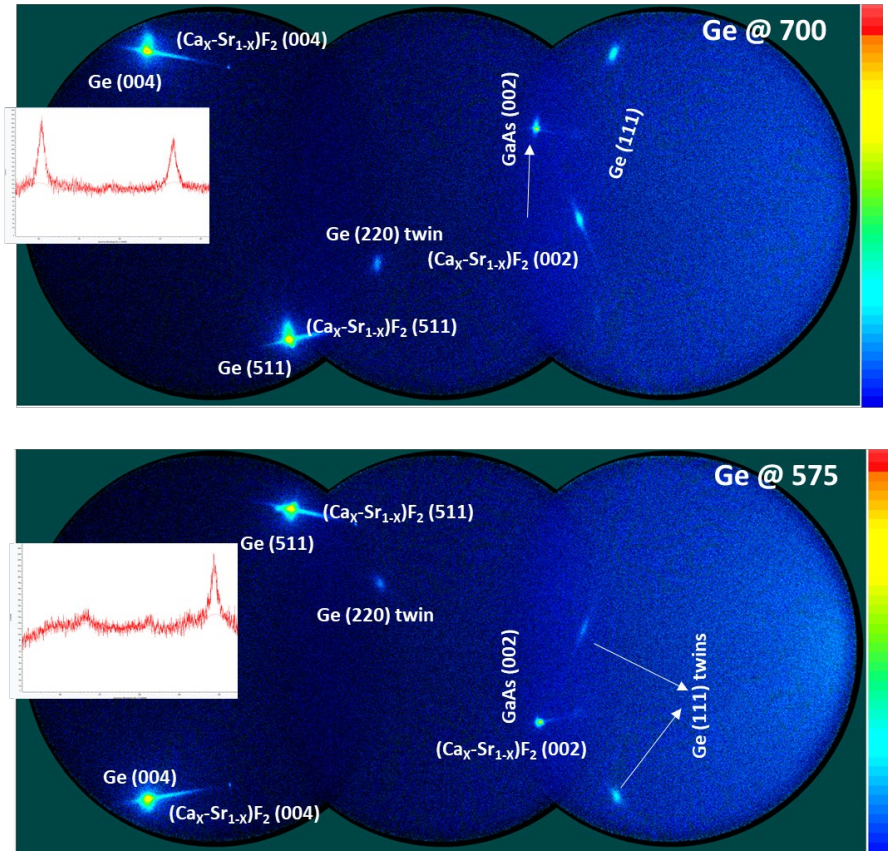

Figure 41. *2D-XRD data showing epitaxial growth of Ge at 700°C (above) and 575°C (below) on $(Ca_X\text{-}Sr_{1-X})F_2/BaF_2/(Ca_X\text{-}Sr_{1-X})F_2$ buffer architecture on (511) GaAs wafer. The inset indicates the intensity of Ge (111) twins.*

GaAs grown on the vicinal substrates required different conditions than that used for (00l) substrates. GaAs growth at 600°C (Figure 42(left)) showed good texture and a smooth morphology. GaAs at 650°C (Figure 42(right)), which is the temperature used for device growth, resulted in a rough film morphology. At higher temperatures, there appears to have been a transition to a mixed growth mode leading to a rough morphology, instead of a layer-by-layer growth mode at lower temperature. This is due to the adatoms detaching from the surface steps caused by the increased adatom movement at higher temperatures.

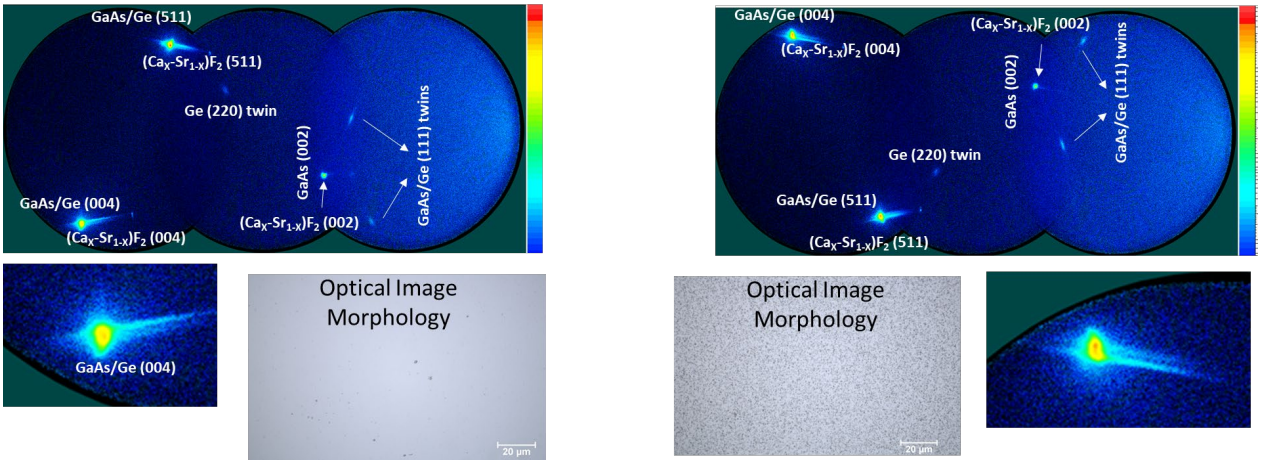

Figure 42. *2D-XRD data and microstructure of GaAs grown at at 600°C (left) and 650°C (right) on (Ca$_X$-Sr$_{1-X}$)F$_2$/BaF$_2$/(Ca$_X$-Sr$_{1-X}$)F$_2$ buffer architecture on (511) GaAs wafer.*

Initial control reference device on vicinal GaAs (511)B substrate showed lower performance (14%) compared to 00L reference solar cell (20%). As shown in Figure 43, GaAs solar cell with fluoride ELO architecture on vicinal substrate showed 95% of the device performance of a corresponding reference 511B device. This presents an opportunity to improve GaAs baseline performance on 511B substrate.

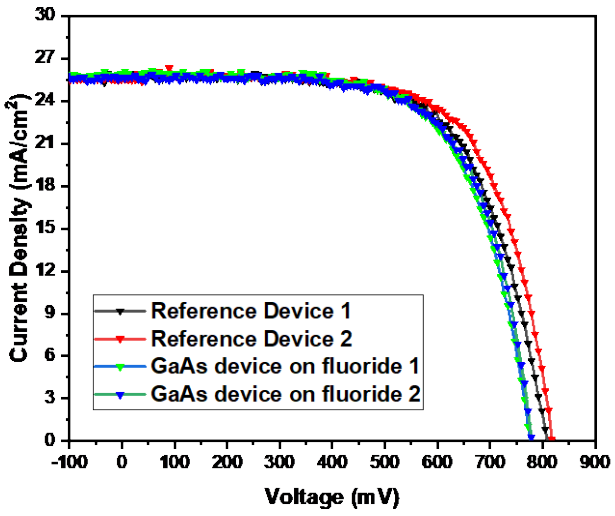

Device	Voc (mV)	J_{SC} (mA/cm^2)	FF	Efficiency (%)
Reference 1	822.45	26.07	0.63	13.65
Reference 2	810.5	25.80	0.68	14.27
Fluoride Buffer 1	775.24	25.92	0.66	13.45
Fluoride Buffer 2	778.09	25.68	0.67	13.5

Figure 43. *Illuminated I-V curves of single junction GaAs solar cells on reference GaAs (511) wafer and on ELO fluoride buffer on (511) wafer. Key PV parameters are shown in the table below.*

GaAs solar cells fabricated on fluoride buffers on (511) wafers also showed good retention of performance after ELO. As shown in Figure 44, devices lifted off the (511) substrates and transferred to Kapton substrate showed a conversion efficiency of ~12% with essentially no degradation of the original device performance.

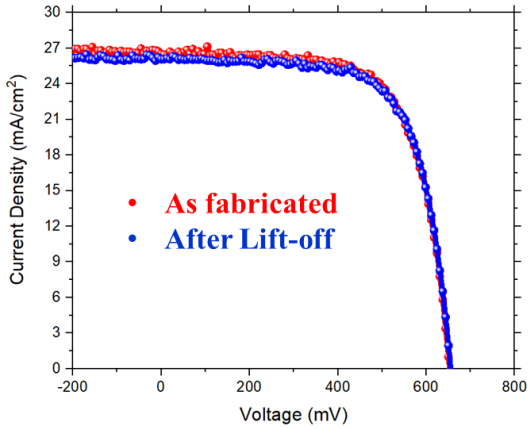

Performance	As fabricated with ARC	After ELO
Voc (mV)	653.1	652.4
J_{SC} (mA/cm²)	26.77	26.41
F.F.	0.69	0.688
Efficiency (%)	12.06	11.86

Figure 44. *Illuminated I-V curves of single junction GaAs solar cells on fluoride buffer on (511) wafer before and after ELO to flexible substrate. Key PV parameters are shown in the table below.*

As shown in Figure 45, the performance of solar cells fabricated on ELO fluoride buffers on (511) wafer is comparable to that of solar cells fabricated directly on (511) substrate. We optimized the doping conditions in GaAs device growth to improve the performance of devices on (511) wafers. Significant improvements in open circuit voltage (820 mV to 900+ mV) and fill factor (67% to 82%) were achieved. Figure 45 shows improvement in the conversion efficiency of devices on (511) wafers to more than 19% after ARC-- this is comparable with the performance of our solar cells on standard (00l) wafers.

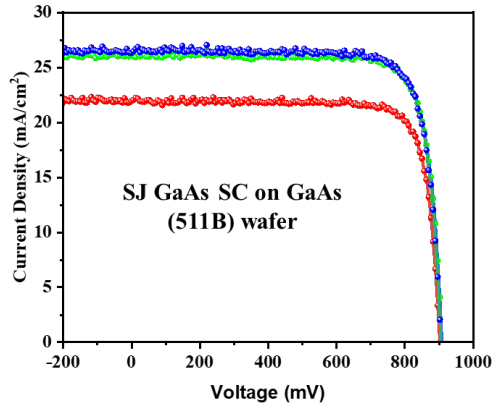

Device	Voc (mV)	J_{SC} (mA/cm²)	FF	Efficiency (%)
As fabricated	896.07	21.90	0.83	16.33
ARC	905.47	25.95	0.81	19.14
ARC	899.48	26.27	0.82	19.40
ARC	902.74	26.10	0.82	19.38

Figure 45. *Illuminated I-V curves of single junction GaAs solar cells directly on (511) wafer before (red curve) and after ARC. Key PV parameters are shown in the table below.*

Results from the best single junction solar cells on fluoride ELO architecture on (511) substrate are shown in Figure 46. The devices' leakage current was in range of 10^{-7} A. The best device with ELO structure showed a power conversion efficiency of 15.60%, with a V_{OC}, Jsc, and fill factor of 719.28mV, 26.53mA/cm^2, and 75%, respectively with ARC.

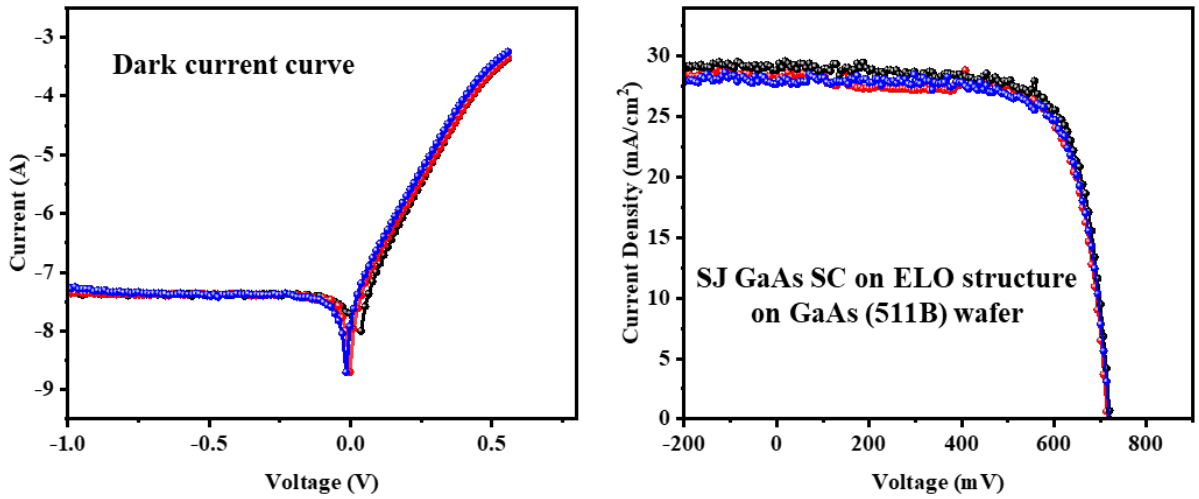

Device	Voc (mV)	J_{sc} (mA/cm^2)	FF	Efficiency (%)
1	712.86	26.29	0.73	14.92
2	719.28	26.53	0.75	15.60
3	715.74	25.51	0.75	14.93

Figure 46. *Dark (left) and Illuminated (right) I-V curves of single junction GaAs solar cells after ARC on on ELO fluoride buffer on (511) wafer. Key PV parameters are shown in the table below.*

Milestones status

1.1.1 NaCl presence with (200) orientation intensity greater than 90% of sum intensity of all NaCl peaks in architecture confirmed. (completed)

1.1.2 Thickness of all layers determined for successful epitaxial lift-off. Porosity of NaCl determined for successful epitaxial lift-off. (completed - using BaF_2 instead of NaCl)

1.2.1 Less than 10% relative reduction in conversion efficiency of 10% without ARC after epitaxial layer lift-off. (completed)

1.3.1 15% efficient solar cells without ARC with less than 10% relative reduction in conversion efficiency after 10 substrate re-uses without CMP. (11% efficiency

demonstrated in solar cells with water-soluble ELO architecture, without ARC. Less than 2% reduction in conversion efficiency after 3 substrate reuses without CMP.)

1.4.1 20% efficient solar cells with ARC on reference architecture. (completed)

1.4.2 20% efficient solar cells with ARC using ELO architecture. (15.6% efficient solar cells demonstrated using water-soluble ELO architecture)

D.1 Results of project presented in technical conference. (completed)

D.2 Results of project submitted for publication. (completed)

Impact: The highest solar cell efficiencies have been achieved with III-V photovoltaics (PV). Still, the use of III-V materials in terrestrial applications has been very limited, mainly because of their high cost. The high cost is primarily due to the expensive Ge or GaAs wafers which could amount up to **one-half of the total module cost!** A prominent approach to reduce the impact of the high cost of substrates used for III-V PV is through re-use of the wafer substrates by Epitaxial Lift-Off (ELO). Typically, using a sacrificial layer such as AlAs, the device part of the cell is lifted off [7, 8], leaving behind the substrate for re-use for fabrication of the next device. While efficiency as high as 29.1% has been achieved by ELO method [9], chemical mechanical polishing (CMP) of the substrate is required after a few re-uses which significantly adds to the overall solar cell cost. *It is estimated that CMP contributes nearly $10/W which is as high as the substrate cost [10].*

By elimination of the CMP process which is the highest cost component of III-V solar cells made by ELO method (~$10/W), and decreasing the substrate cost by 100X (by 100 re-uses), the proposed technology will be a big leap forward in significantly reducing the cost of III-V photovoltaics. The low module costs, reduced BOS costs and longer life time could together enable III-V PV reach the 2030 SunShot Utility goal of $0.03/kWh.

References:

1. M. Barkai, E. Grünbaum, and G. Deutscher. "The epitaxial growth of Ge single-crystal films on a CaF_2/sapphire substrate." *Journal of Vacuum Science & Technology A: Vacuum, Surfaces, and Films* **9.5** 2642-2647 (1991)
2. L. J. Schowalter et al. “Strain in epitaxial GaAs on CaF_2/Si (111)” *Journal of Vacuum Science & Technology B: Microelectronics Processing and Phenomena*, **8,** 246-249 (1990).
3. W. Li, W, T. Anan and L. J. Schowalter “Optimization of GaAs epitaxy on CaF_2/Si (111) substrates” *Journal of crystal growth*, **135,** 78-84 (1994).
4. W. Li, W, T. Anan and L. J. Schowalter “Nucleation of GaAs on CaF_2/Si (111) substrates” *Applied physics letters*, **65,** 595-59 (1994).
5. W. Li, W, T. Anan, T. Thundat and L. J. Schowalter, “Initiation and Evolution of Epitaxial Growth of GaAs on CaF_2/Si (111) Substrates” *MRS Online Proceedings Library Archive*, *317* (1993).

6. A. N. Tiwari et al. “Metalorganic vapor phase epitaxy of GaAs on Si using IIa-flouride buffer layers” *Journal of crystal growth*, **124,** 565-569 (1992).
7. M. Konagai, M. Sugimoto and K. Takahashi, “High efficiency GaAs thin film solar cells by peeled film technology” *J. Cryst. Growth* **45,** 277–280 (1978).
8. C-W. Cheng, K-T Shi, N. Li, S-J. Han, L. Shi and D. K. Sadana, “Epitaxial lift-off process for gallium arsenide substrate reuse and flexible electronics”, *Nature Communications* **4,** 1577 (2013)
9. https://www.altadevices.com/technology/
10. Horowitz, Kelsey A. W., Timothy Remo, Brittany Smith, and Aaron Ptak. 2018. “Techno-Economic Analysis and Cost Reduction Roadmap for III-V Solar Cells” Golden, CO: National Renewable Energy Laboratory. NREL/TP-6A20-72103. https://www.nrel.gov/docs/fy19osti/72103.pdf.

Budget and Schedule:

Federal share: $200,000 (all spent according to plan)

Cost share: $50.000 (all spent according to plan).

Project start date: March 1, 2020

Project end date: August 31, 2021

Project was completed on schedule without extensions.

Path Forward:

Research needs to be continued on improving the efficiency of GaAs devices fabricated on water-soluble buffers. Specifically, the defect density in these devices needs to be reduced. Then multi-junction devices need to be demonstrated on water-soluble templates.

Inventions, Patents, Publications, and Other Results:

1. S. Sharma, C. A. Favela, B. Yu, E. Galstyan, S. Sun, T. Terlier, and V. Selvamanickam “From Salt to Electronics: Heteroepitaxy and GaAs Solar Cells” *Advanced Materials Interfaces* 2201148 (2022).
2. S. Sharma, C. A. Favela, B. Yu, E. Galstyan, and V. Selvamanickam, “Conversion efficiency improvement of ELO GaAs solar cell, deposited on water soluble sacrificial buffer” *Surface & Coatings Technology (submitted).*
3. S. Sharma, C. Favela, S. Sun, and V. Selvamanickam, “Novel Epitaxial Lift-Off for Flexible, Inexpensive GaAs Solar Cells” 47th IEEE Photovoltaics Specialist Conference (virtual), June 14 – 18, 2020.

4. S. Sharma, “Flexible & Inexpensive III-V Photovoltaics”, *Society of Vacuum Coaters Techcon,* Long Beach, CA, April 30 – May 5, 2022.
5. S. Sharma, “Flexible GaAs Solar Cell Using Water-Soluble Sacrificial Layer for Epitaxial Lift-Off Process” *49th IEEE Photovoltaics Specialist Conference,* Philadelphia, PA, June 5 - 10, 2022.